

Bayesian Time-of-Flight for Realtime Shape, Illumination and Albedo

Amit Adam¹ Christoph Dann² Omer Yair¹ Shai Mazor¹ Sebastian Nowozin³

¹Microsoft AIT - Advanced Imaging Technologies, Haifa, Israel

²School of Computer Science, CMU, Pittsburgh PA

³Microsoft Research - Cambridge, Cambridge UK

Abstract—We propose a computational model for shape, illumination and albedo inference in a pulsed time-of-flight (TOF) camera. In contrast to TOF cameras based on phase modulation, our camera enables general exposure profiles. This results in added flexibility and requires novel computational approaches. To address this challenge we propose a generative probabilistic model that accurately relates latent imaging conditions to observed camera responses. While principled, realtime inference in the model turns out to be infeasible, and we propose to employ efficient non-parametric regression trees to approximate the model outputs. As a result we are able to provide, for each pixel, at video frame rate, estimates and uncertainty for *depth*, *effective albedo*, and *ambient light intensity*. These results we present are state-of-the-art in depth imaging. The flexibility of our approach allows us to easily enrich our generative model. We demonstrate that by extending the original single-path model to a two-path model, capable of describing some multipath effects. The new model is seamlessly integrated in the system at no additional computational cost. Our work also addresses the important question of optimal exposure design in pulsed TOF systems. Finally, for benchmark purposes and to obtain realistic empirical priors of multipath and insights into this phenomena, we propose a physically accurate simulation of multipath phenomena.

Index Terms—Time-of-flight, Bayes, depth cameras, intrinsic images, multipath



1 INTRODUCTION

The commercial success of depth cameras in recent years has enabled numerous computer vision applications. Notable applications are human pose estimation [1, 2], dense online 3D reconstruction of an environment [3], and other uses—an overview is available in a recent special issue [4] and in the review article [5].

Broadly speaking we may differentiate between depth cameras based on triangulation and cameras which estimate depth based on time of flight (TOF) [6, 7]. Furthermore, while in the context of TOF the cameras often operate using modulated illumination and sensing, and the computational methods usually employ phase-space reasoning [7], in this paper we take a different approach which we now describe.

Figure 1 describes the inputs and outputs of our system. We start with n concurrently captured intensity images obtained under active illumination of the scene, using n different exposure profiles. Using these n observations at every pixel, we infer the depth, reflectivity, and ambient lighting conditions. We achieve this by using a generative probabilistic model that relates the unknown imaging conditions—*shape*, *illumination* and *albedo*—to the per-pixel camera observations. To perform

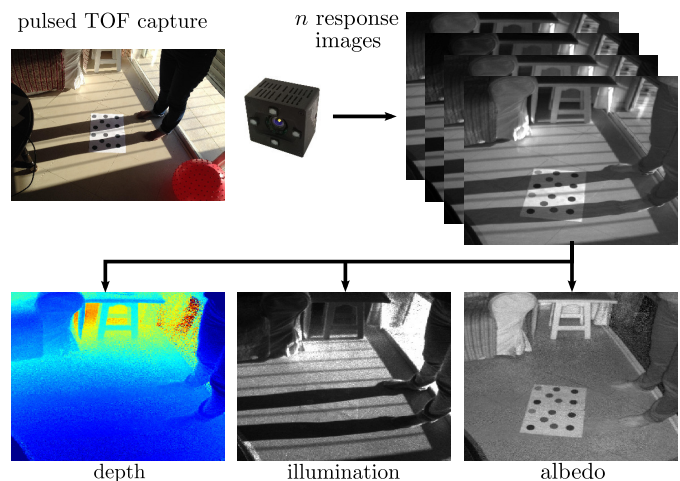


Fig. 1: System overview: the inputs are n pulsed TOF response images, obtained concurrently using different exposure profiles. In realtime (30fps) we separate *depth*, *ambient illumination* and *effective albedo* at every pixel.

inference we use either Bayesian inference or maximum likelihood estimation.

However, achieving realtime video rate by direct application of these inference methods is infeasible under practical constraints on computation. Therefore we use an approach inspired by model compression [8] and approximate the accurate but slow inference methods using regression trees, a fast non-parametric regression method [9].

The regression approach has two advantages; first,

it allows to approximate inference in principled probabilistic models under tight compute and memory constraints; second, it decouples the model from the runtime implementation, allowing continuing improvements in the model without requiring changes to the test-time implementation.

We demonstrate this important advantage in Section 5 where we extend our generative model to a richer model which considers multipath effects. Our decoupling of model+inference from runtime regression allows us seamless switching between different generative models, at no additional computational cost. To the best of our knowledge no other depth cameras have used a statistical regression approach for online depth inference.

No matter which model we use for inference, at times there will be pixels that the model fails to explain. Common reasons are mixed pixels (imaging a depth discontinuity), sensor saturation, complex multipath, interference from another active device, or extreme image noise. We propose a robust fit-to-model score that can be used to detect and invalidate affected pixels from further processing.

Having described inference and pixel invalidation, we address an orthogonal but important question in pulsed TOF systems: exposure profile design. We are flexible to choose exposure profiles and we directly optimize the expected accuracy of inferred depth using Bayesian decision theory. This yields a challenging optimization problem and we propose an approximate solution.

Finally, we introduce an accurate TOF simulation procedure based on physically accurate light transport simulation. We use this capability for both exposure design and for synthetic but physically accurate benchmarking.

1.1 Related Work

Most commercially available time-of-flight cameras (as of early 2015) work using *modulated* time of flight [10, 11], also known as *phase-based* time-of-flight. They generate a sinusoidal illumination signal and measure correlation of the reflected signal with a sinusoidal-profiled gain function of the same frequency, delayed by a phase shift [12]. For a fixed frequency and phase shift a recorded frame does not contain sufficient information to reconstruct depth. Therefore, modern systems typically record a sequence of frames at multiple frequencies and multiple phase shifts and use the combined set of frames to unambiguously infer depth using so called *phase unwrapping* algorithms [7, 12].

In contrast, our camera uses *pulsed* TOF, also known as *gated* TOF. This technology has differentiators in terms of hardware-related aspects (size, power, resolution) which are not relevant here, but let us highlight an important computational aspect of this camera: in contrast with the sine-like gain functions used in modulated TOF, we are allowed to choose from a large space of possible gain functions. Hence more general inference methods are required.

Our work on optimizing the gain profiles has not been addressed in pulsed TOF systems, but for modulated TOF prior work [13] has attempted to optimize the illumination profile to improve depth accuracy.

Shape, Illumination, and Reflectance. Recovering the imaging conditions leading to a specific image—the inverse problem of imaging, is a long standing goal of computer vision. A recent modern treatment of this problem has been given in [14, 15, 16, 17], with a comprehensive historical review. Conceptually the approach in these works is similar to ours: find the most likely shape, illumination and albedo to give rise to the observed image. In contrast with these works, we do the inference at the pixel level and not the image level, being able to do so due to the unique imaging process we employ. Additionally our regression approach allows this inference to be done in realtime. Moreover, our shape output actually gives the full posterior depth distribution. This allows direct usage of our depth in incremental estimators or integrators such as [3] that specifically take care to maintain the state distribution at all times [18, 19].

In the context of illumination estimation, we remark that there have been specific works on shadow removal [20, 21], which is a nice byproduct of our approach (see Figure 1).

Multipath Interference. Multiple reflections (multipath) commonly occur in real scenes [6]. There is now a solid body of work on handling multipath in modulated TOF systems, but to the best of our knowledge there is no published work on handling multipath in pulsed TOF cameras.

We briefly discuss work that exists for modulated TOF and relate it to our proposed solution. The work of [22, 23] and [24] model the light reflections in the scene globally to improve depth inference. To do this, they assume planar Lambertian surfaces and iteratively minimize an energy function. The methods work in important settings but the expensive minimization procedure precludes a realtime implementation. The work [25, 26, 27] assumes two-path interference from close-to-specular surfaces. The resulting methods are practical and efficient and our approach in Section 5 makes similar model assumptions. However, we work with different signals (pulsed TOF) and also provide a probabilistic model with uncertainty estimates. The work [28] generalizes the above two-path models to signals which arise from either two-path specular or two-path Lambertian reflectors; these signals are “compressible” and can hence be described with few parameters; the resulting method can be implemented in real time. Another recent branch of literature originating from work on transient imaging [29] uses modulated TOF imaging with Fourier-based reconstruction of the time-dependent light density. The work of [30, 31] reconstructs the transient light density for each pixel from a large number of modulated TOF images, each with a different modulation frequency. While this line of work could inspire practical multipath techniques and is

computationally efficient, currently the large number of required frequencies (several dozen) and the large acquisition time precludes realtime applications in dynamic scenes.

The robust invalidation of observations seems to have not been considered before with the exception of [28] who provide an adhoc method for invalidation. Because we use a sound probabilistic model we can leverage and adapt standard methods in Bayesian practice [32] for this purpose.

1.2 Contributions

To summarize and as an aide in following the paper, our novel contributions are:

Principled Framework

- A probabilistic generative model for pulsed TOF imaging;
- Principled inference of all latent imaging conditions, given camera observations
- Accurate depth uncertainty estimates;
- Robust Bayesian per-pixel invalidation for outlier observations;

Practicalities

- A novel use of regression to enable realtime inference under tight compute and memory constraints;
- Complete decoupling of runtime mechanism from model and inference

Extensibility and Multipath

- A probabilistic model for depth inference in the presence of simple multi-path;

Results

- Experimental results showing robust video-rate inference of shape, illumination and reflectance, both indoors and outdoors at direct sunlight;

Computational Photography and Tools

- Design of exposure profiles to directly optimize depth accuracy under task-derived imaging conditions;
- A novel physically-based renderer for TOF simulation
- Use of the simulator for both exposure design and benchmarking

2 MODELING THE IMAGING PROCESS

We start with our camera’s principle of operation, then formulate a generative model relating the unknown imaging conditions to the observable camera outputs. Assume that a specific pixel images a point at a certain distance and denote by t the time it takes light to travel twice this distance. The reflected signal is integrated at the pixel using a gain determined by a shutter signal $S(\cdot)$. If $P(\cdot)$ is the emitted light pulse, the reflected pulse arriving after time t is $P(u - t)$. The observed response due to the reflected light pulse is

$$R_{\text{active}} = \int S(u) \rho P(u - t) d(t) du. \quad (1)$$

Here ρ denotes the effective reflectivity¹ of the imaged point, and $d(t) = \frac{1}{t^2}$ denotes decay of the reflected pulse due to distance. Therefore, the reflected pulse is down-scaled by a factor of $\rho d(t)$. The quantity $\rho P(u - t)d(t)$ is integrated with an exposure-determined gain $S(\cdot)$.

Let us now consider the effect of ambient illumination. We denote by λ the ambient light level falling on the imaged point. Then the reflected light level is $\rho\lambda$, and we assume that during the integration period, this level of ambient light is constant. Therefore, the observed response due to ambient light is $R_{\text{ambient}} = \int S(u) \rho\lambda du$. The actual observed response is the sum of the responses due to active illumination and due to ambient light,

$$R = \int S(u) (\rho P(u - t) d(t) + \rho\lambda) du. \quad (2)$$

Equation (2) specifies the relationship between the unknown imaging conditions (t, ρ, λ) (depth, albedo, and ambient light level), and the observation we obtain at the pixel, when using the exposure profile $S(\cdot)$. We *concurrently* use n different exposure profiles² $S_1(\cdot), S_2(\cdot), \dots, S_n(\cdot)$, and obtain n observations as

$$\begin{bmatrix} R_1 \\ \vdots \\ R_n \end{bmatrix} = \rho \begin{bmatrix} \int S_1(u) P(u - t) d(t) du \\ \vdots \\ \int S_n(u) P(u - t) d(t) du \end{bmatrix} + \rho\lambda \begin{bmatrix} \int S_1(u) du \\ \vdots \\ \int S_n(u) du \end{bmatrix} \\ = \rho \vec{C}(t) + \rho\lambda \vec{A}. \quad (3)$$

In short, we have the observed response vector

$$\vec{R} = \rho \vec{C}(t) + \rho\lambda \vec{A}. \quad (4)$$

Here $\vec{C}(t)$ is the expected response from a point at distance equivalent to time t , assuming unit reflectivity and no ambient light. This response is scaled by the reflectivity ρ and shifted in the ambient light direction \vec{A} , the magnitude of the shift being the product of albedo and ambient light level. Equation (4) is the model describing our imaging process.

We remark that $\vec{C}(\cdot)$ and \vec{A} are determined by the illumination and exposure signals and are estimated using a simple camera calibration process which is outside the scope of this paper.

Figure 2 shows the curve $\vec{C}(\cdot)$ as a function of depth t , for a typical exposure profile design. The four colored curves denote the specific response curves of four exposure profiles $S_1(\cdot), \dots, S_4(\cdot)$, namely

$$C_i(t) = \int S_i(u) P(u - t) d(t) du. \quad (5)$$

Looking at Figure 2, consider the response vector \vec{R} we may expect from depth $t = 150\text{cm}$. We see that the first (blue) coordinate should be high, the second and fourth

1. We use both the terms albedo and reflectivity. The quantity ρ we use in the model actually contains the effect of foreshortening and therefore we refer to effective reflectivity/albedo.

2. The hardware system enabling concurrent different exposure profiles is described in [33] and [34, 35].

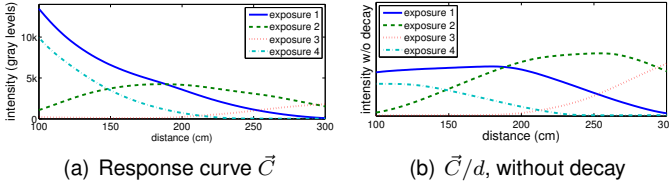


Fig. 2: A typical response curve. (a) The actual curve $\vec{C}(\cdot)$. As distance grows the response decays, as per equation (5). (b) Decay-compensated response where we plot $\vec{C}(t)/d(t) = t^2\vec{C}(t)$ for more details (from now on we use decay-compensated curves for visualization).

coordinates should be approximately equal and the third coordinate (red) should be the lowest. In contrast, at depth $t = 190\text{cm}$ the first and second entries of \vec{R} should be approximately equal (blue and green). Thus we see that by suitable design of the curve $\vec{C}(\cdot)$, we may expect to be able to infer depth accurately using the responses we observe.

Since the response we observe is scaled by the albedo ρ , it may be tempting to normalize the response vector. However, as we discuss in the next section, the noise *does* depend on the magnitude and therefore the unnormalized response contains relevant information for depth inference and for predicting depth uncertainty that would be lost upon normalization.

3 A PROBABILISTIC MODEL

We now rephrase (4) as a probabilistic model, relating the imaging conditions (t, ρ, λ) to a distribution over responses \vec{R} . Specifically we model \vec{R} given t, ρ, λ as

$$\vec{R} \sim P(\vec{R} | t, \rho, \lambda), \quad (6)$$

where we assume that $P(\vec{R} | t, \rho, \lambda)$ is a multivariate Gaussian distribution with mean vector as in (4),

$$\mathbb{E}[\vec{R} | t, \rho, \lambda] = \vec{\mu}(t, \rho, \lambda) = \rho \vec{C}(t) + \rho \lambda \vec{A}, \quad (7)$$

and with a diagonal covariance matrix

$$\Sigma(\vec{\mu}) = \begin{pmatrix} \alpha\mu_1 + K & & & \\ & \ddots & & \\ & & \ddots & \\ & & & \alpha\mu_n + K \end{pmatrix}. \quad (8)$$

Here K is related to *read noise*—noise that is part of the system even when no light is present. The affine relationship between the magnitude of the response and its variance is due to *shot noise* and is well known [36, 37]. We validate this noise model experimentally in the supplementaries.

The generative model (6) is the distribution of the observed \vec{R} at a pixel given the imaging conditions. We would like to *infer* the imaging conditions depth t , reflectivity ρ and ambient light level λ given the observation \vec{R} . There are three mainstream approaches for doing so, namely Bayesian posterior inference, maximum likelihood estimation (MLE), and maximum a posteriori (MAP) estimation.

3.1 Bayesian Inference

We assume certain priors on depth, reflectivity and ambient light level, denoted by $p(t)$, $p(\rho)$, and $p(\lambda)$. In addition we assume independence between these factors. Let us focus on inferring depth t , the most relevant unknown for depth cameras. Bayes rule gives

$$\begin{aligned} P(t | \vec{R}) &\propto P(\vec{R} | t) p(t) \\ &= p(t) \iint P(\vec{R} | t, \rho, \lambda) p(\rho) p(\lambda) d\rho d\lambda. \end{aligned} \quad (9)$$

Equation (9) gives the posterior distribution over the true unknown depth. We get the posterior density up to a normalization factor which may be extracted by integrating over every possible t . The posterior density is the ideal input to higher level applications which use probabilistic models [18, 19]. For other applications, it may be sufficient to summarize this posterior distribution by a point estimate, for example the posterior mean $\hat{t}_{\text{Bayes}}(\vec{R}) = \mathbb{E}[t | \vec{R}]$ or the MAP depth $\hat{t}_{\text{map}}(\vec{R}) = \text{argmax}_t P(t | \vec{R})$, together with a measure of the dispersion such as the posterior variance.

Computationally, we have to solve the integration problem (9) at every pixel. Doing this at frame rate under low compute resources is currently not feasible.

A second issue with (9) is that it requires the specification of priors $p(t)$, $p(\rho)$, and $p(\lambda)$. While using uniform priors on depth and reflectivity is physically plausible, specifying the prior on ambient light level is harder. For example, operating the camera in a dark room versus a sunlit room, would require very different priors. If the used prior deviates too much from the actual situation our estimates of depth could be biased, that is, suffer from systematic errors.

3.2 Maximum Likelihood Inference (MLE)

Alternatively we use maximum likelihood estimation for the imaging conditions,

$$(\hat{t}_{\text{mle}}, \hat{\rho}_{\text{mle}}, \hat{\lambda}_{\text{mle}}) = \text{argmax}_{t, \rho, \lambda} P(\vec{R} | t, \rho, \lambda). \quad (10)$$

Instead of considering the depth that accumulates the most probability over all reflectivity and ambient light explanations, we consider the single combined imaging conditions $(\hat{t}_{\text{mle}}, \hat{\rho}_{\text{mle}}, \hat{\lambda}_{\text{mle}})$ which have the highest probability of producing the observed response \vec{R} .

3.3 Maximum A Posteriori Inference (MAP)

This method is the most likely point estimate taking into account prior preferences. We obtain it similar to the MLE estimate as

$$(\hat{t}_{\text{map}}, \hat{\rho}_{\text{map}}, \hat{\lambda}_{\text{map}}) = \text{argmax}_{t, \rho, \lambda} p(t) p(\rho) p(\lambda) P(\vec{R} | t, \rho, \lambda). \quad (11)$$

The optimization problems (10) and (11) are non-linear because $\vec{\mu}(\cdot)$ is non-linear and because our noise

model (8) has a signal-dependent variance. An iterative numerical optimization is required and a frame rate resolution at every pixel is infeasible. We discuss further details of the inference procedures for MLE, MAP, and Bayesian inference in the supplementary materials.

4 A REGRESSION TREE APPROACH

All inference methods we propose, MLE \hat{t}_{mle} , MAP \hat{t}_{map} , and Bayesian inference \hat{t}_{Bayes} produce reliable depth estimates. However the computation of these estimates is expensive and impractical for a realtime camera system. To perform realtime inference we use a regression approach to approximate the model as follows.

- 1) **Offline:** Sample imaging conditions (t_i, ρ_i, λ_i) from the prior and responses \vec{R}_i from the model (6). Then use one of the slow inference methods to generate labeled training data $(\vec{R}_i, \hat{t}(\vec{R}_i))$.
- 2) **Offline:** Train a regression tree/forest using the training data set, to obtain a predictor \hat{t}_{RF} .
- 3) **Online:** Given an observed response \vec{R} predict the inferred depth $\hat{t}_{\text{RF}}(\vec{R})$.

Why would this procedure be a good idea?

- First, \hat{t}_{mle} , \hat{t}_{map} , and \hat{t}_{Bayes} are smooth functions from the response space to depth and are simple to learn.
- Second, the regression tree \hat{t}_{RF} has small performance requirements in terms of memory and computation.
- Third, it decouples the runtime from future changes to the probabilistic model and inference procedures.

In principle it would be desirable to train directly on a large and diverse corpus of ground truth data captured from the real world; however, capturing ground truth depth data is challenging [38], expensive, and ensuring the diversity in imaging conditions is difficult. Training on our forward model instead allows us to represent a wide variety of imaging conditions. Likewise, while we could train directly on samples (\vec{R}_i, t_i) from the model this would incur additional variance because the noise makes \vec{R} stochastic even for a fixed depth value. By training on the estimator (\vec{R}, \hat{t}_i) instead we effectively remove this variance from the regression task.

For learning the regression tree we use the standard CART sum-of-variances criterion in a greedy depth first manner [9]. For the interior nodes of the trees we perform binary comparisons on the individual responses, $R_i \leq a$. At each leaf node b we store a linear regression model,

$$\hat{t}_b(\vec{R}) = \theta_b^T \cdot [1, R_1, \dots, R_n, R_1^2, R_1 R_2, \dots, R_n^2]^T, \quad (12)$$

where we use a quadratic expansion of the responses. We estimate the parameters θ_b of each leaf model using least squares on all training samples that reach this leaf [39].

We cannot over emphasize the practical importance of a flexible and decoupled-from-model regression scheme, in handling unexpected or new phenomena. An example is detailed in the supplementaries.

Approximation Tradeoffs. Because of its non-parametric nature the regression tree or forest can approach the quality of the exact inference output if given sufficient training data and expressive power. However, the key limiting factor in our actual implementation are specific constraints on available memory and compute. Basically the depth of the tree and the structure of the leaf predictor, determine the memory requirements. In Section 9 we example the accuracy vs memory tradeoffs experimentally.

4.1 Additional Regression Outputs

In addition to the estimated depth we output several other quantities per pixel. These outputs too are produced using trained regression trees. Specifically, we produce the following additional outputs:

- Reflectivity, $\hat{\rho}$, using $\mathbb{E}[\rho|\vec{R}]$ or via (10), (11).
- Ambient light level, $\hat{\lambda}$, using $\mathbb{E}[\lambda|\vec{R}]$ or via (10), (11).
- Depth uncertainty, as described below.
- Fit-to-model invalidation score γ , for detection of irregular imaging conditions, described in Section 6.

4.2 Computing Depth Uncertainty

In many applications of depth cameras to computer vision problems the estimated depth is used as part of a larger system; in these applications it is useful to know the uncertainty of the depth estimate. One example would be surface reconstruction [3], where uncertainty can be used to weight individual estimates and to average them over time.

We use the variance of the depth, in the form of a *standard deviation* $\hat{\sigma}(\vec{R})$, as a measure of uncertainty. Depending on whether we use \hat{t}_{Bayes} or \hat{t}_{mle} , we compute the standard deviation as follows.

For \hat{t}_{Bayes} we use the posterior distribution (9), and directly compute $\hat{\sigma}_{\text{Bayes}}(\vec{R}) = \sqrt{\mathbb{V}_{t \sim P(t|\vec{R})}[t]}$.

For \hat{t}_{mle} in (10), we employ the approach described in [40]. A first order Taylor expansion of the gradient (wrt imaging conditions) of the likelihood function in (10) is used to relate a perturbation $\Delta\vec{R}$ in the response to the resulting perturbation of the estimator $\hat{t}_{\text{mle}}(\vec{R} + \Delta\vec{R})$. This analysis leads to the covariance matrix of the maximum likelihood estimator and an approximation to the standard deviation, $\hat{\sigma}_{\text{mle}}(\vec{R}) = \sqrt{\mathbb{V}[\hat{t}_{\text{mle}}]}$.

In Section 9 and Figure 8(b) we demonstrate the accuracy of our uncertainty estimates by comparing them with the actual observed uncertainty. In the context of phase-based TOF, previous work [41] used random forests to output depth confidence scores for measured phase signals; their regressor was trained using laser scans. Here we instead obtain uncertainty directly from our probabilistic model.

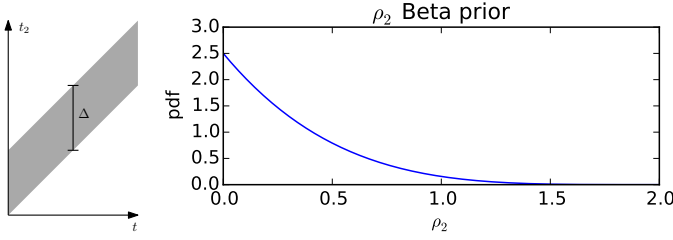


Fig. 3: Two-path model priors for the additional latent variables t_2 and ρ_2 . Left: The prior for the second bounce depth t_2 is uniform over the shaded polygon. Right: the prior for ρ_2 is defined over $[0; 2]$ in order to handle large diffuse reflectors.

5 TWO-PATH MODEL FOR SIMPLE MULTIPATH

The generative model (4) we used so far assumed a single direct response from the point being imaged. In order to account for multipath, this model needs to be extended as to describe the additional multipath light being integrated at the pixel. We demonstrate a simple extension of the model and inference as follows.

Consider a two-path model as proposed in [25, 26, 28]. In addition to the three unknowns t , ρ , and λ , we now also assume a second contribution having travelled depth $t_2 > t$, from a patch with reflectivity ρ_2 . We extend the generative model (7) to

$$\vec{\mu}_2(t, \rho, \lambda, t_2, \rho_2) = \rho \left(\vec{C}(t) + \lambda \vec{A} + \rho_2 \vec{C}(t_2) \right), \quad (13)$$

where ρ scales both the direct and indirect response, and ρ_2 scales only the indirect response. The model is exact for a second specular surface, but becomes an approximation in case the second surface is diffuse. For inference we extend the inference procedures to this model in a straightforward manner (details in the supplementaries).

For the prior of t_2 we select a uniform prior relative to t , such that $t_2 - t$ is uniform between 0cm and Δ (typically $\Delta = 150\text{cm}$), that is,

$$p(t_2|t) = \mathcal{U}(t_2; t, t + \Delta). \quad (14)$$

For the second reflectivity we allow $\rho_2 > 1$ to be able to handle diffuse surfaces, and after studies of simulation data select a Beta distribution on the interval $[0; 2]$.

$$p(\rho_2) = \mathcal{B}(\rho_2/2; \alpha = 1, \beta = 5). \quad (15)$$

This prior specifies that values up to $\rho_2 = 2$ are possible, but that low values of ρ_2 are more likely. Both priors are visualized in Figure 3 and we will evaluate this model on real and simulated data in the experiments section.

It is important to emphasize that our regression-decoupled-from-model approach allows us to seamlessly use this extended model in the camera, just by plugging it in the offline step 1 of the procedure outlined at the beginning of Section 4. The runtime process and its computational cost do not change at all.

6 BAYESIAN MODEL INVALIDATION SCORE γ

Our imaging model is an idealization of the real world and in each frame a certain number of pixels will have measured responses \vec{R} which do not conform to this model. The main reasons for this are systematic errors such as multipath [22, 28], pixels of mixed depth, sensor saturation, as well as statistical extremes in imaging noise. In Section 5 we extended our model to explain some multipath effects, but even this extended model may fail to explain some of the responses.

When our model fails to accurately explain the observed response vector \vec{R} we would like to detect such a deviation from the model assumptions and exclude affected observations from further processing. The strict Bayesian paradigm cannot detect deviation from model assumptions because it only provides the calculus to go from assumptions and observations to conclusions and no mechanism to falsify the assumptions themselves [42]. However, in Bayesian modelling practice [43] a common method to assess deviations from model assumptions is to perform so called *posterior predictive checks*.

We use the posterior predictive p-value [32, 44, 45] for our purposes. Intuitively our particular p-value will measure the total probability mass of all observations which have a smaller likelihood than the likelihood of the observed response. Therefore the score is always between zero and one and a value close to zero indicates that the observation is unlikely under the assumed model. This intuition is helpful but the controversy around p-values and model checking more generally is deep and we give a brief discussion in the supplementary materials.

To formalize this problem, let us first unify notation by writing $\theta = (t, \rho, \lambda)$ or $\theta = (t, \rho, \lambda, t_2, \rho_2)$, depending on whether we use the single path model (7) or the two path model (13), so that θ are all the unknown imaging conditions to be inferred. Given an observed response vector \vec{R} and using the model $P(\vec{R}|\theta)$ and the prior $P(\theta)$ we can use Bayesian inference to infer the posterior distribution $P(\theta|\vec{R})$. Following the above intuition the invalidation score γ is defined as

$$\gamma(\vec{R}) = \mathbb{E}_{\theta \sim P(\theta|\vec{R})} \left[\mathbb{E}_{\vec{R}' \sim P(\vec{R}'|\theta)} \left[\mathbb{1}_{\{P(\vec{R}'|\theta) \leq P(\vec{R}|\theta)\}} \right] \right], \quad (16)$$

Here we used the notation $\mathbb{1}_{\{\text{predicate}\}}$ which evaluates to one if the predicate is true and to zero otherwise. The above equation integrates all probability mass of less likely observations, weighted by the posterior $P(\theta|\vec{R})$. If we have many repetitions of the experiment $\theta \sim P(\theta)$ and $\vec{R} \sim P(\vec{R}|\theta)$ the scores $\gamma(\vec{R})$ would be uniformly distributed. The computation of (16) is essentially free during our approximate Bayesian inference procedure.

The value $\gamma(\vec{R})$ can be used to reject the null hypothesis of the assumed model: if $\gamma(\vec{R}) \leq \tau$ for some threshold τ we reject the assumed model for this observation. The score (16) is also applicable to MLE and MAP inference if

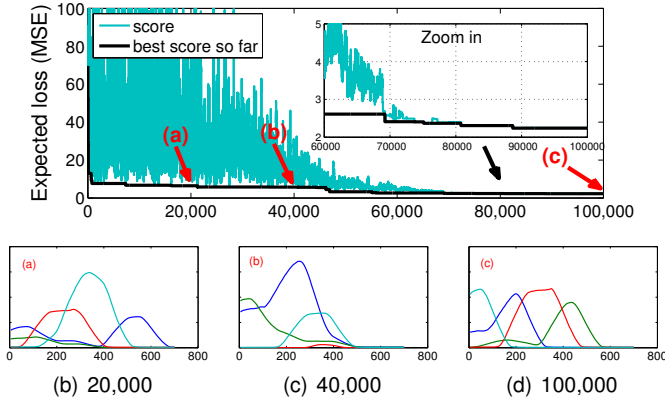


Fig. 4: Exposure profile optimization. **Top:** Simulated annealing over 100k iterations, finding response curves to minimize (19), the expected error (MSE) in depth estimation. **Bottom:** snapshots of the response curves after 20k, 40k, and after all 100k iterations. The x-axis is depth (cm).

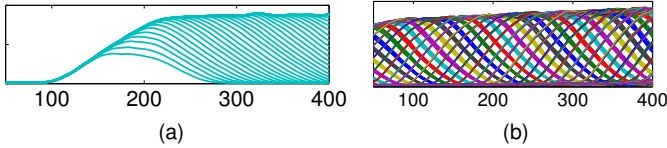


Fig. 6: **Left**, (a): basis functions $\{Q_j/d\}$ for a fixed delay δ and varying width w . **Right**, (b): all basis functions $\{Q_j/d\}_{j \in J}$, defined by Eq. (17).

we replace the outer expectation by a unit point mass at the inferred imaging conditions $\hat{\theta}_{\text{mle}}$ or $\hat{\theta}_{\text{map}}$, respectively. We evaluate the invalidation score experimentally in Section 9.7.

7 EXPOSURE PROFILES DESIGN

So far we covered our imaging model, our realtime regression approach and how we can invalidate responses unlikely to have been generated by our model. We now turn to an orthogonal question of designing a suitable response curve \vec{C} for use in (4) (\vec{A} is closely related to \vec{C} and are both derived from \mathbf{Z} which will immediately be defined). Recall from (5) that \vec{C} is the integral of the illumination pulse P with the exposure profile S . In the camera, a laser diode and driver produce the illumination pulse P , and its design is fixed. The exposure gain S , however, has a flexible design space parameterized by linear basis functions. We would like to design response curves \vec{C} that will produce observations from which low-error estimates of the imaging conditions could be inferred.

The camera is able to use basic exposure gain profiles in the form of a boxcar function, as shown in Fig. 5. Each basic gain profile has two parameters: a delay δ , and a width w . Each possible pair $j = (\delta, w)$ specifies one possible gain profile B_j from a fixed discrete set of choices J . Typically the set J contains several hundred possible combinations. With (5) we now get the basis

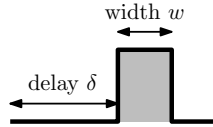


Fig. 5: A basis element $j = (\delta, w)$ defining $B_j(\cdot)$.

function Q_j associated to B_j as convolution with the pulse,

$$Q_j(t) = \int B_j(u) P(u-t) d(t) du. \quad (17)$$

Fig. 6 shows a set of basis functions for all possible $j \in J$. We represent the basis response curves as vectors $Q_j \in \mathbb{R}^T$, for a time discretization with T values. By stacking the $m = |J|$ vectors horizontally we obtain a matrix $\mathbf{Q} \in \mathbb{R}^{T \times m}$ containing all possible basis response curves. The possible design space represents each curve as linear combination of basis curves, that is $S(\cdot) = \sum z_j B_j(\cdot)$. With (17) we then obtain the combined response curve $C(\cdot) = \sum z_j Q_j(\cdot)$. To design not just one but n response curves $S_i(\cdot)$ for $i = 1, \dots, n$, we represent the design space using a matrix $\mathbf{Z} \in \mathbb{R}^{m \times n}$ as

$$\mathbf{C} = \mathbf{Q} \mathbf{Z}, \quad (18)$$

where in $\mathbf{C} \in \mathbb{R}^{T \times n}$ the k 'th column contains the response for the k 'th exposure sequence.

For the design objective we utilize *statistical decision theory* [46] to select \mathbf{Z} to optimize the expected quality of depth inference. There are two components to this idea: the quality measure, and the expectation. The quality of depth inference is measured by means of a *loss function* which compares an estimated depth \hat{t} with a known ground truth depth t to yield a quality score $\ell(\hat{t}, t)$. One possible loss function which we use is the squared error, $\ell(\hat{t}, t) = (\hat{t} - t)^2$, but we can also use other functions, for example $\ell_t(\hat{t}, t) = \ell(\hat{t}, t)/t$. For the expectation, as for the Bayesian depth inference, we devise priors, typically uniform, $p(t)$, $p(\rho)$, and $p(\lambda)$ over the unknowns. Then the design problem is

$$\underset{\mathbf{Z}}{\text{argmin}} \quad \mathbb{E}_{t, \rho, \lambda} \mathbb{E}_{\vec{R} \sim P(\vec{R}|t, \rho, \lambda, \mathbf{Z})} \left[\ell(\hat{t}(\vec{R}), t) \right] \quad (19)$$

$$\text{sb.t.} \quad \sum_{j=1}^m \sum_{i=1}^n Z_{ji} \leq K_{\text{shutter}}, \quad (20)$$

$$\sum_{j=1}^m 1_{\{Z_{ji} > 0\}} \leq K_{\text{sparsity}}, \quad i = 1, \dots, n, \quad (21)$$

$$Z_{ji} \in \mathbb{N}, \quad j = 1, \dots, m, i = 1, \dots, n,$$

where the notation $1_{\{\text{pred}\}}$ evaluates to one if the predicate is true and to zero otherwise.

The constraints (20) and (21) deserve some comments. Each captured frame contains a fixed number K_{shutter} of light pulses, each of which is associated with a basic exposure signal B_j . These are assigned in integer units. The total number of basis functions that can be used is constrained by K_{sparsity} due to various shutter driver restrictions. Because in each pulse a single basis function is selected, this makes the effective response curve \mathbf{C} a non-negative linear combination of the basis functions.

Solving (19) is a challenging combinatorial problem on three levels: first, computing $\hat{t}(\vec{R})$ is the inference problem, which has no closed form solution. Second, as a result, computing the expectations also has no closed form solution. Third, more than just merely evaluating it, we would like to optimize the objective function over \mathbf{Z} .

The approximate solution which we adopt is as follows (more details in the supplementary materials). We

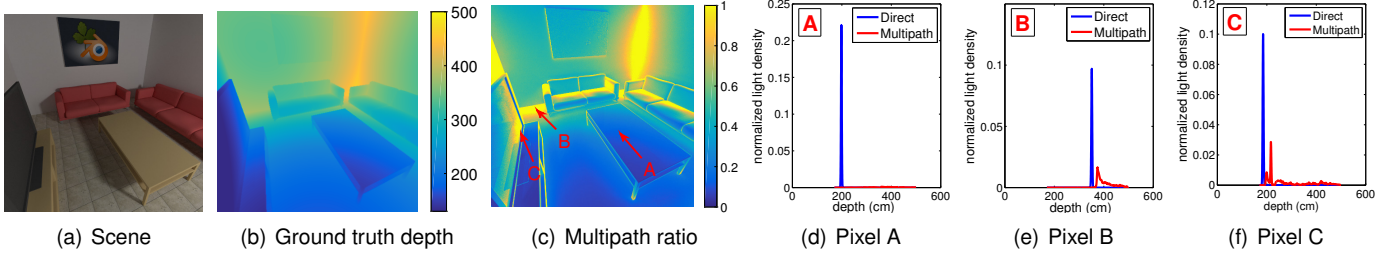


Fig. 7: Insights into multipath using physically accurate light transport simulation. (a) A scene created in Blender. (b) Ground truth depth. (c) Normalized measure of multipath intensity compared to direct contributions. (please see the main text). (d)-(f) Normalized light densities for three selected pixels; pixel A has no multipath component, pixel B has one multipath component from 30–50cm further away, and pixel C, where a specular component gives rise to a narrow multipath response.

approximate the objective function by a Monte Carlo evaluation for both expectations (imaging conditions, and responses): for $i = 1, \dots, K$ we draw t_i, ρ_i, λ_i , then draw \vec{R}_i , then perform inference to obtain $\hat{t}_i = \hat{t}(\vec{R}_i)$ and evaluate $\ell_i = \ell(\hat{t}_i, t_i)$. Finally we approximate the objective (19) as empirical mean $\frac{1}{K} \sum_{i=1}^K \ell_i$. For $K = 8192$ samples this computation takes around one second. For optimization of (19) we use simulated annealing [47] on a custom-designed Markov chain which respects the structure induced by (20) and (21).

Figure 4 shows the progress of the optimization process. We start the optimization at a completely closed exposure profile with zero gain, that is $Z_{ji} = 0$ for all j, i .

We remark that the optimization scheme just described outperforms all our previous attempts to manually design the exposure profiles.

8 MULTIPATH MODELING AND DESIGN

In this section we describe our method for simulating realistic multipath images together with ground truth. Having a realistic simulation enables several important goals:

- exposure design for reduced multipath artifacts
- learning/obtaining realistic priors for multipath effects
- benchmarking

We show results for the first and last goal in section 9.

8.1 Time of Flight Simulation

In computer graphics physically-accurate renderers are mature technology that are readily available. We adapt the open source *Mitsuba renderer* [48]. Mitsuba supports, based on physical modeling of light scattering, light transport simulation, integrating paths of light at every pixel, thereby producing a highly realistic rendered image. We adapt the code so that we obtain the total light path length and the number of segments of the light trajectory.

In more detail, we modify two rendering algorithms, the bidirectional path tracer algorithm [49] and the Metropolis light transport (MLT) [50] algorithm; normally both algorithms are used to render the intensity of

a pixel by means of approximating an integral over light pathes connecting light sources to surfaces to camera pixels [51].

Our modification is to record for each pixel a weighted set of light path samples $\{(w_i, L_i, t_i)\}_{i=1, \dots, N}$, typically a few thousand, say $N = 4096$. For each light path we store the intensity weight $w_i \geq 0$, the number of straight path segments $L_i \in \mathbb{N}$, and the total length of the path t_i . The segment count allows us to distinguish direct responses ($L_i = 2$, emitter-to-surface and surface-to-camera) from indirect responses ($L_i > 2$, multipath). Together with a fixed ambient value τ measuring light intensity without active illumination, for example from a regular rendering pass, the path lengths and weights now permit us to simulate a realistic mean response vector $\vec{\mu}$ as

$$\vec{\mu} = \tau \vec{A} + \sum_{i=1}^N \frac{w_i}{d(t_i)} \vec{C}(t_i). \quad (22)$$

The sum in the second term approximates the time-of-flight integral $\int_{\mathbb{R}_+} \vec{C}(t) d\nu(t)$, where ν is an intensity measure over time. The division by $d(t_i)$ is due to both w_i and \vec{C} containing the distance decay function $d(t)$; see (5). Once we have $\vec{\mu}$ we can optionally simulate sensor noise as specified in (8). We provide details in the supplementaries.

We remark that additional relevant work on light transport is considered in [52, 53], published independently and concurrently with our work.

8.2 Simulation Results

In part (a) of Figure 7 we show a synthetic scene. Part (b) shows the ground truth depth map corresponding to the scene. We marked three points (A, B and C shown in part 7(c)) at which we have different amounts of multipath. In parts 7(d), 7(e), and 7(f) we show the depth histograms we obtain from our modified Mitsuba renderer. For every point, the histogram shows the distribution of distances travelled by the photons integrated at this pixel. This distribution is properly weighted to account for both distances and reflectivity of materials along the pathes. Furthermore we show the distribution of distances travelled over a direct path in blue (this essentially corresponds to a delta function), and distances travelled over multiple pathes in red. We see that at point A (part 7(d)) there is no multipath, while at point B (part 7(e)) there is multipath due to the wall.

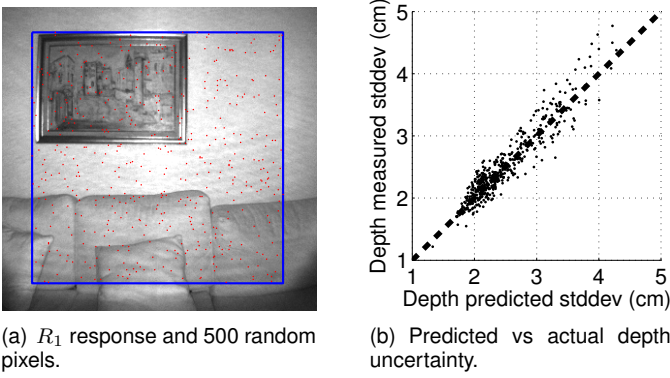


Fig. 8: Predicted uncertainty versus actual uncertainty; the model is well-calibrated in that it accurately predicts depth uncertainty.

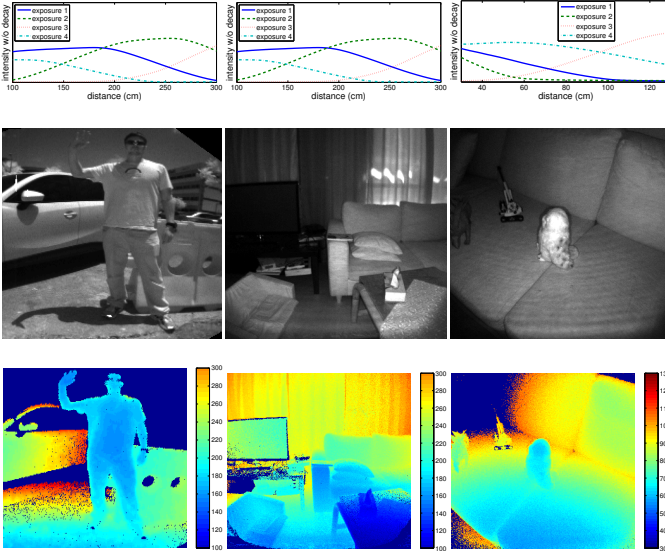


Fig. 9: Sample scenes. **Top**: exposure profile used. **Middle**: first response image R_1 . **Bottom**: inferred depth image using the SP-MLE model. The left and middle column are scenes with a far-range design, the right column is a scene with a near-range design. The designs were obtained using different priors $p(t)$ in (19).

We may see from the histogram the dominant additional path lengths - 30 to 50 cm in this case. Finally, in part 7(c) we show a normalized measure of the percentage of intensity integrated from multipath (as opposed to intensity integrated from a single direct light path), for every pixel in the image. We see that corners and just in front of the wall or other vertical surfaces actually return more multipath signals than direct path signals.

8.3 Multipath-Robust Exposure Profile Design

In the exposure profile design objective (19) we take two expectations: the first over prior imaging conditions (prior p) and the second over the assumed forward model (forward model P , equation (6)). This indeed is the way to minimize the loss when responses come from our basic generative model, which does not include multipath.

We now want to design an exposure profile that will be more resistant to multipath. Therefore we should measure the loss over responses that also include multipath. We use our realistic simulator for that as follows. Given one or multiple 3D scenes and their realistic light transport paths, we sample responses from these scenes. Formally, the scenes and the simulator are a more complex generative model G . We denote the sampling from this complex model by $(\vec{R}, t) \sim G$, but do keep in mind that the model G uses multiple reflectivity values and ambient lighting along the paths to generate the response \vec{R} . Both P and G depend on the design \mathbf{Z} through (7) and (22), respectively.

We combine both generative models in a mixture: a fraction $\beta \in [0; 1]$ are samples from our assumed model prior p and P , and a fraction $1 - \beta$ are samples from the physical simulation prior Q . Then the expectation (19) becomes

$$\beta \mathbb{E}_{t, p, \lambda \sim p} \mathbb{E}_{\vec{R} \sim P} [\ell(\hat{t}(\vec{R}), t)] + (1 - \beta) \mathbb{E}_{(\vec{R}, t) \sim G} [\ell(\hat{t}(\vec{R}), t)]. \quad (23)$$

We see that the design objective (19) can, by a simple change as in (23), accommodate richer priors over scenes and effects such as multipath. We demonstrate this in section 9.5.

9 EXPERIMENTAL RESULTS

We use a prototype camera as shown in Figure 1. In our experiments we avoid reference and comparison with other depth cameras in terms of noise characteristics and variance of depth estimates because the validity of such comparison is affected by hardware configurations such as power used, field of illumination, resolution, thermal design constraints, and sensor sensitivity. Instead we focus on demonstrating the validity of our model, inference procedures, and regression approximations.

Throughout the experiments we will use the abbreviations SP and TP to refer to the single-path model (6) and the two-path model (13), respectively. Depending on the inference method we use MAP, MLE, and Bayes, so that TP-Bayes for example means the two-path model with full Bayesian inference.

9.1 Sample scenes

We start with a few sample scenes shown in Figure 9. We designed two exposure profiles using two different uniform priors on depth $p(t)$ in (19). The first prior focused on larger depths while the second prior focused on smaller ranges. The two left columns show outdoor and indoor scenes using the far range exposure profile, and the right column shows a scene captured with the short range profile. The middle row shows the first response image, and the bottom row shows the inferred depth (obtained using the regression tree).

9.2 Accurate Depth Uncertainty

Next we show that by accurately modeling the noise present in the observed response our model is able to

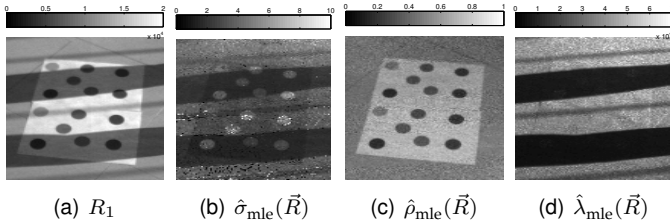


Fig. 10: Posterior inference results under different illuminations and albedos. (a) First response image, exhibiting varying ambient light levels and albedos, including strong shadows. (b) Posterior depth uncertainty (cm), higher under either stronger ambient light or lower albedo. (c) Inferred albedo map, in $[0; 1]$. (d) Inferred ambient illumination map.

assess its own uncertainty in the inferred depth. To demonstrate this we capture 200 frames of a static scene as shown in Figure 8(a) and sample 500 pixel locations in the shown box.

Since the camera is static, we can obtain the empirical standard deviation of the depth estimators for each of the 500 points. We plot this empirical depth uncertainty, against the predicted uncertainty obtained in the first frame as described in Section 4.2 (the predicted uncertainty is nearly identical over all 200 frames). Figure 8(b) shows the good agreement between the predicted uncertainty and the actual uncertainty. This provides empirical data about how well the model is *calibrated* [54], that is, how accurately it judges the uncertainty in its own predictions.

To gain some insight on what determines depth standard deviation, we turn to Figure 10, showing a part of the scene shown in Figure 1. In Fig. 10(a), we see one of the input responses, showing the combined effect of different albedos and shadows. In Fig. 10(b) we see how imaging conditions affect the variance of the depth estimates. In the shadowed regions the ratio between the active illumination and ambient light is higher, and this generally leads to a tighter posterior. On materials with higher albedo (the white page vs the dark circles) the amount of reflected light is higher and this also leads to smaller variances (as compared with the variances on dark circles which reflect less light). In addition, the depth itself affects the measure of uncertainty but this is not illustrated in this zoomed scene.

9.3 Ambient and Effective Reflectivity

In our model, the inferred albedo image is illumination-invariant and therefore does not contain shadows. Therefore we can perform realtime shadow removal [20, 21], providing illumination-invariant inputs to computer vision algorithms. This is illustrated in Fig. 10(c). In Fig. 10(d) we show the estimated ambient light level at each pixel.

For more results on realtime extraction of illumination, reflectivity and shape please view the enclosed video.

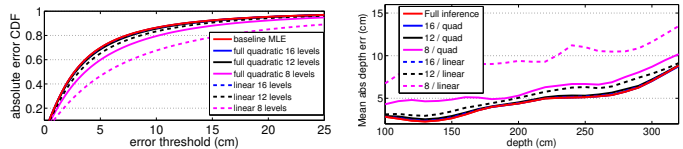


Fig. 11: Regression tree errors compared to full inference. **Left:** Cumulative error distribution over test set. **Right:** mean absolute error over prior albedo and ambient levels.

9.4 Regression Tree Approximation Quality

As discussed we use regression trees to regress depth, thus approximating full inference which is infeasible in realtime. An optimized implementation running on a *Intel HD Graphics 4400 GPU*, evaluates a regression tree of depth 12 with full quadratic polynomials on a 200-by-300 pixel frame in 2.5ms. This means we are able to run four trees (depth, illumination, albedo and depth std) effectively at ≈ 100 fps. The enclosed video shows this implementation running (the std was computed but not shown in the output windows).

We now quantify the additional errors incurred due to the use of regression trees instead of full inference. The added error depends on the tree structure, which determines required memory resources as described in section 4. We tested two types of trees at three depths, yielding six possible tree structures. The two types of trees used either a linear polynomial or a quadratic polynomial on the leaves. The depths we used were 8, 12 and 16 (full binary trees).

After training the trees, we generate test data by sampling from the prior imaging conditions and our generative model (6). We compute the baseline error by running full inference (in this case MLE, but similar results hold for Bayes) on the test data, then run the various tree predictors. Fig. 11 shows the results. On the left we plot the cumulative distribution of errors over the test set. On the right we partition the test set by depths, and show the mean absolute error for each depth, averaged over all albedos and illumination levels. We see that as the trees get deeper the quality approaches that of the full inference. At 16 levels they essentially match.

9.5 Design for Multipath Robustness

Now we demonstrate how we may use our simulator for obtaining exposure profiles designed to be robust to multipath. In section 8.3 we allowed for more complex generative models during exposure profile design, one that will generate responses that are “contaminated” by multipath. We took two simple scenes of an object in front of highly reflective wall (scene provided in supplementaries) and used them as the model Q as in section 8.3. For the mixture model we used $\beta = 0.5$. We then ran our design optimization scheme to obtain a new exposure profile. Let us call this exposure profile the MP-resistant design. We compare it with the standard design

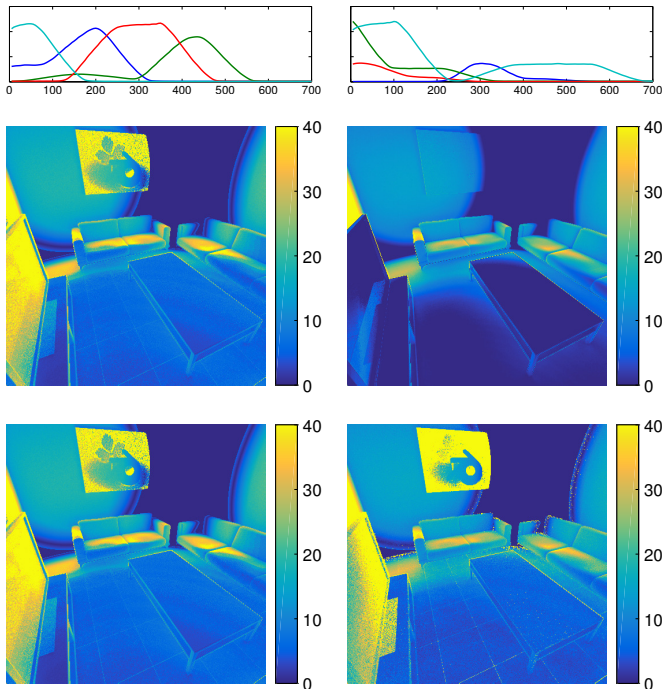


Fig. 12: Multipath-robust exposure profile design. **Left column**: original exposure profile. **Right column**: multipath-optimized exposure profile. **From top-to-bottom**: *Top*; regular exposure profile and robust-to-multipath profile. *Middle*; bias magnitude (cm) of resulting depth inference images. *Bottom*; Simulated RMSE (cm) including noise.

obtained using $\beta = 1$. The two designs are tested on the scene shown in Fig. 7. We emphasize that this test scene is different than the scene used in design. Fig. 12 compares the results we obtain. The top row shows the regular design on the left, and the MP-resistant design on the right (obtained using two different values of β in (23)). The second row shows the magnitude of the resulting depth bias. On the left we see significant biases due to multipath (compare with the multipath map in Fig. 7(c)). With the MP-resistant design we see a significant reduction in bias. The bottom row shows the expected RMSE under both designs. Please note that this RMSE contains the jitter in the estimates due to pixel shot noise. In temporal integration procedures like [3] this error diminishes, and therefore it is more important to have the bias reduced than have this RMSE reduced.

9.6 Experimental Verification of Simulation Accuracy

Our light transport simulation is based on an accurate physical model of light and the simulation results should agree with the real camera. However, a real time-of-flight camera is a complex system with many components and potentially unaccounted for interactions between them. In this section we verify that our simulation serves as a good proxy for the real system.

To this end, we take images from two real scenes with a box and an optional reflector, shown in Figure 13(a) and 13(h), keeping the camera static between captures.

We then perform *camera mapping* using the known camera intrinsics and reconstruct a matching 3D scene for our simulator. The synthetic scene allows us to assess the agreement between qualitative effects in the real capture and in the synthetic image. In our comparison we mask the results to the area occupied by the box and reflector, and in addition mask the bottom third of the sensor array because this particular camera has no active illumination design in this region.

The top row in Figure 13 shows the scene with only the box, the bottom row shows the multipath-corrupted scene with a large diffuse reflector added.

The following important observations can be made: 1. Comparing each of the four pairs of real and synthetic results the qualitative and quantitative error agree between the actual recording and the simulation; 2. The multipath corruption is clearly visible for the single-path (SP) model in Figure 13(k) and 13(l) and to a smaller extent in the two-path (TP) models, Figure 13(m) and 13(n).

Overall the simulation agrees very well with the real camera system. We remark that beyond this single experiment we describe here, the simulator is in daily use in our group and we have seen excellent agreement between simulated results and live tests over many months of using it.

9.7 Robust Model Invalidation

To demonstrate the performance of the proposed invalidation mechanism we use the same real experimental data as in the previous section. We compute the γ score for both scenes and for the SP-Bayes and TP-Bayes models.

The results are shown in Figure 14 and show that robust invalidation is possible for this scene. In the next section we also report γ score images for simulation data.

9.8 Benchmarking using Simulation Data

In this final experiment we leverage the ability of our simulator to provide ground truth depth. This allows us to assess the depth inference performance quantitatively. We use five scenes adapted from blendswap.com for this purpose. The depth range in each of these scenes is within 50cm to 500cm and the scene surfaces represent a good variety in materials and convex and concave geometries.

The results are visualized in Figures 15 to 16 and we report quantitative results for depth reconstruction in Table 1. Two additional visualizations are provided in the supplementary materials. As error metric we use the 25/50/75 quantiles of absolute depth errors because these approximately correspond to easy/medium/difficult surfaces. We mask pixels in white for which no direct single-path response is created during rendering. These pixels typically correspond to either infinite rays or to perfectly specular surfaces. In

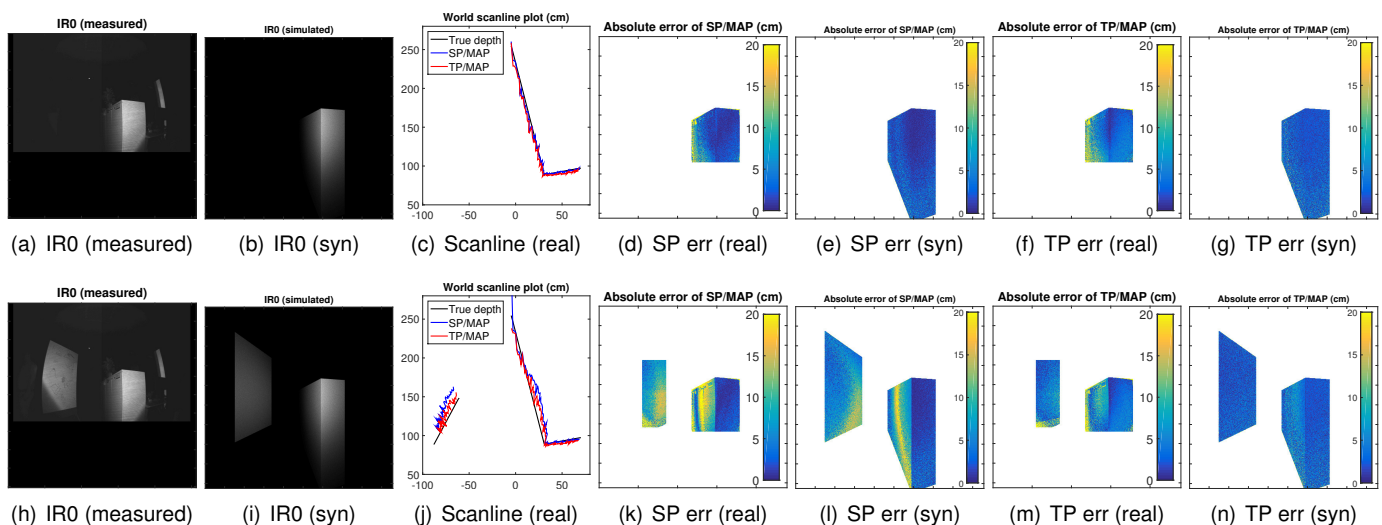


Fig. 13: Validation of the accuracy of light transport simulation. From the measured IR0 frames we use camera mapping to approximately reconstruct the 3D scene geometry and surface properties manually. The top row shows the no-multipath setting and we mask the frame so that only the target object is shown. The bottom row shows the multipath setting with a large white reflector added to the scene (left side). In the error results, each column corresponds to either real errors from the measured IR frames or is entirely simulated. Qualitatively there is an excellent agreement between real measurements and synthetic simulations. Small quantitative differences remain, for example in the no-multipath setting with the two-path model.

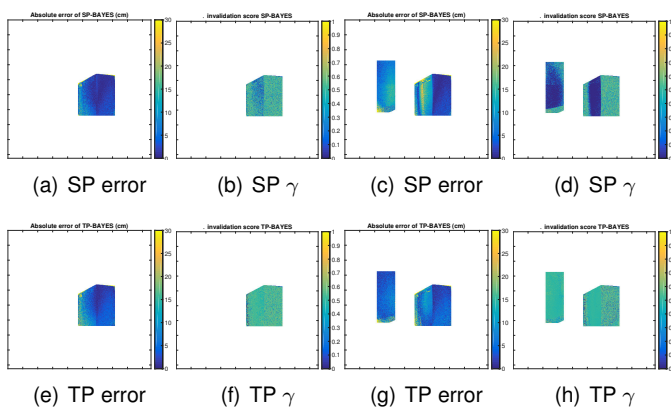


Fig. 14: Robust invalidation of measurements that violate our model assumptions, as explained in Section 6. In the top row we show the single path model SP-Bayes depth inference errors on real data as with the previous experiment in Section 9.6, whereas the bottom row shows the TP-Bayes model. The γ invalidation score robustly highlights pixels affected by multipath in (d) (values close to zero in dark blue) leading to large depth errors in (c). By thresholding the γ score at a suitably chosen threshold these measurements can be excluded from further processing. Note that the two-path (TP) model handles multipath and the γ score in (h) does not invalidate affected pixels.

both cases the time-of-flight operating principle does not apply.

We again re-emphasize that the absolute magnitude of the errors is not material and incomparable to other cameras for two reasons: first we report raw-depth errors with absolutely no spatial or temporal filtering that is usually present. Second, the jitter error highly depends on camera power, sensor size and other hardware characteristics which are of no concern in this paper.

From the results we make the following observations:

- 1) Surfaces with low reflectivity have large depth errors but the model is aware of this through a large inferred $\hat{\sigma}$ value. For example, the black

floor in Figure 15(d) and 15(e), or the cooking stove in Figure 16(e). Improving on these regions would require increasing the light output or sensor sensitivity.

- 2) Areas affected by strong multipath also have large depth errors; for example the ceiling in Figure 15(d). The SP model $\hat{\sigma}$ does not indicate a potential error, but the γ score can invalidate these observations, for example the ceiling in Figure 15(f).
- 3) The two-path model (TP) improves depth accuracy in every scene but also reports increased model $\hat{\sigma}$ compared to the single-path model. For example, compare the absolute errors between Figures 15(d) and 15(j), and the $\hat{\sigma}$ maps in Figure 15(e) and 15(k).
- 4) Less invalidation happens in the two-path model. In all scenes, the TP-Bayes γ invalidates less pixels compared to the SP-Bayes γ map, because as a model it is a better representation for the physical simulator.
- 5) In Table 1 the errors are significantly reduced by the two-path model, typically by 40 percent.

These results and insights agree with extensive live tests performed in the process of productizing our system.

10 CONCLUSION

Our presented approach is based on sound probabilistic modelling given our understanding of the physical reality. Bayesian inference naturally provides a powerful formal calculus to perform depth inference given our modelling assumptions. We have shown that even a simple model of multipath enables significant reductions in the depth error. However, both parts of our approach—the *prior* and *model*—are general and open to future extensions. For the prior we plan to develop scene- and

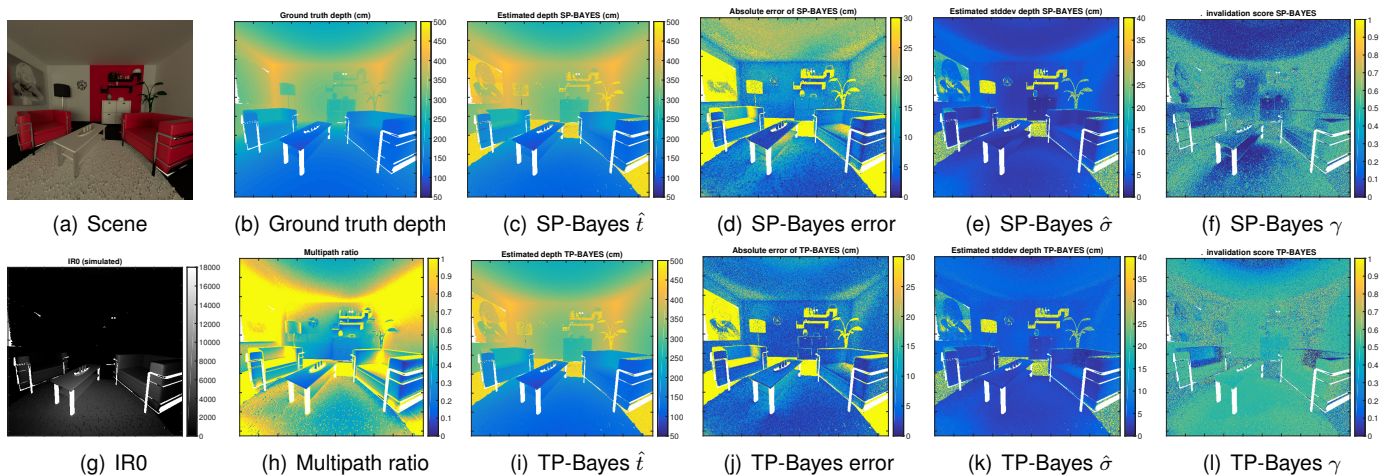


Fig. 15: Rendered simulation (scene adapted from “sitting room” by cenobi, licensed CC-BY from blendswap.com). High errors are present due to low reflectivity surfaces and multipath; the multipath errors are reduced by the two-path model (ceiling, wall, floor). The uncertainty estimate $\hat{\sigma}$ is higher for the two-path model, reflecting the multipath awareness (compare the $\hat{\sigma}$ values at the ceiling).

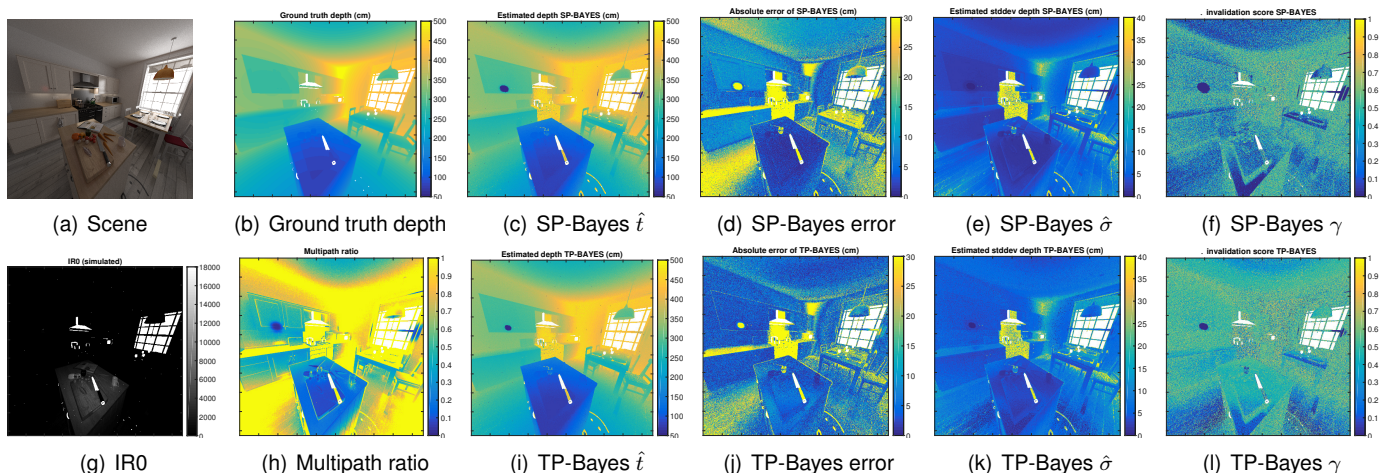


Fig. 16: Rendered simulation (scene adapted from “Country-Kitchen Cycles” by Jay-Artist, licensed CC-BY from blendswap.com). Overall strong multipath error reduction across the scene but higher overall single-frame jitter due to the strong ambient lighting.

Scene	Model	Absolute error quantile (cm)		
		25%	50%	75%
Sitting Room Fig. 15	SP-Bayes	6.43	12.50	20.24
	TP-Bayes	2.89	6.27	11.68
Breakfast Room (supp. mat.)	SP-Bayes	3.09	5.69	10.39
	TP-Bayes	1.60	3.40	6.55
Kitchen Nr 2 (supp. mat.)	SP-Bayes	6.01	10.29	17.26
	TP-Bayes	2.86	6.04	12.65
Country Kitchen Fig. 16	SP-Bayes	4.69	9.63	17.20
	TP-Bayes	2.75	5.87	11.78
Wooden Staircase (supp. mat.)	SP-Bayes	4.08	8.59	14.64
	TP-Bayes	2.19	4.85	9.51

TABLE 1: Predictive performance of the Bayesian single-path (SP) and two-path (TP) models on realistic data obtained from physically-accurate light transport simulation. Across all scenes the 25/50/75 error quantiles are significantly reduced by the two-path model. (raw-depth errors - no spatial or temporal filtering whatsoever)

task-specific priors to be able to improve performance in the presence of strong multipath and ambient light. We envision more refined models of multipath, for example

by replacing the two-path pulse response by a more accurate analytic model of diffuse Lambertian multipath. This would require adding further latent variables related to multipath responses and creating suitable priors for them; this may be challenging but our simulation framework will likely enable us to make progress in this direction in the future. Our statistical view on time-of-flight enables all these extensions within a principled framework.

ACKNOWLEDGMENTS

We thank Michael Baltaxe, Yair Sharf, Sahar Vilan and Giora Yahav for their contributions, long term support and commitment to this work.

Parts of this work have been done when Christoph Dann interned at Microsoft Research Cambridge, UK.

REFERENCES

- [1] J. Shotton, A. W. Fitzgibbon, M. Cook, T. Sharp, M. Finocchio, R. Moore, A. Kipman, and A. Blake, “Real-time human pose recognition in parts from single depth

- images," in *The 24th IEEE Conference on Computer Vision and Pattern Recognition, CVPR 2011, Colorado Springs, CO, USA, 20-25 June 2011*. IEEE, 2011, pp. 1297–1304. [Online]. Available: <http://dx.doi.org/10.1109/CVPR.2011.5995316>
- [2] J. Shotton, R. B. Girshick, A. W. Fitzgibbon, T. Sharp, M. Cook, M. Finocchio, R. Moore, P. Kohli, A. Criminisi, A. Kipman, and A. Blake, "Efficient human pose estimation from single depth images," *IEEE Trans. Pattern Anal. Mach. Intell.*, vol. 35, no. 12, pp. 2821–2840, 2013. [Online]. Available: <http://doi.ieeecomputersociety.org/10.1109/TPAMI.2012.241>
- [3] R. A. Newcombe, S. Izadi, O. Hilliges, D. Molyneaux, D. Kim, A. J. Davison, P. Kohli, J. Shotton, S. Hodges, and A. W. Fitzgibbon, "KinectFusion: Real-time dense surface mapping and tracking," in *10th IEEE International Symposium on Mixed and Augmented Reality, ISMAR 2011, Basel, Switzerland, October 26-29, 2011*. IEEE, 2011, pp. 127–136. [Online]. Available: <http://dx.doi.org/10.1109/ISMAR.2011.6092378>
- [4] L. Shao, J. Han, D. Xu, and J. Shotton, "Computer vision for RGB-D sensors: Kinect and its applications," *IEEE T. Cybernetics*, vol. 43, no. 5, pp. 1314–1317, 2013. [Online]. Available: <http://dx.doi.org/10.1109/TCYB.2013.2276144>
- [5] H. Jungong, S. Ling, X. Dong, and J. Shotton, "Enhanced computer vision with Microsoft Kinect sensor: A review," *IEEE Transactions on Cybernetics*, vol. 43, no. 5, pp. 1318–1334, Oct 2013.
- [6] D. Lefloch, R. Nair, F. Lenzen, H. Schäfer, L. Streeter, M. J. Cree, R. Koch, and A. Kolb, "Technical foundation and calibration methods for time-of-flight cameras," in *Time-of-Flight and Depth Imaging: Sensors, Algorithms, and Applications*. Springer, 2013, pp. 3–24.
- [7] M. E. Hansard, S. Lee, O. Choi, and R. Horaud, *Time-of-Flight Cameras - Principles, Methods and Applications*, ser. Springer Briefs in Computer Science. Springer, 2013.
- [8] C. Bucilă, R. Caruana, and A. Niculescu-Mizil, "Model compression," in *Proceedings of the 12th ACM SIGKDD international conference on Knowledge discovery and data mining*, 2006.
- [9] L. Breiman, J. H. Friedman, R. A. Olshen, and C. J. Stone, *Classification and Regression Trees*. Belmont: Wadsworth, 1984.
- [10] R. Schwarte, Z. Xu, H.-G. Heinol, J. Olk, R. Klein, B. Buxbaum, H. Fischer, and J. Schulte, "New electro-optical mixing and correlating sensor: facilities and applications of the photonic mixer device (PMD)," vol. 3100, 1997, pp. 245–253.
- [11] R. Lange and P. Seitz, "Solid-state time-of-flight range camera," *IEEE Journal of Quantum Electronics*, vol. 37, no. 3, pp. 390–397, 2001.
- [12] M. Gupta, S. K. Nayar, M. B. Hullin, and J. Martin, "Phasor imaging: A generalization of correlation-based time-of-flight imaging," Tech. Rep., 2014.
- [13] A. D. Payne, A. A. Dorrington, and M. J. Cree, "Illumination waveform optimization for time-of-flight range imaging cameras," in *SPIE Optical Metrology*. International Society for Optics and Photonics, 2011, p. 80850D.
- [14] J. T. Barron and J. Malik, "Shape, albedo, and illumination from a single image of an unknown object," in *2012 IEEE Conference on Computer Vision and Pattern Recognition, Providence, RI, USA, June 16-21, 2012*. IEEE, 2012, pp. 334–341. [Online]. Available: <http://dx.doi.org/10.1109/CVPR.2012.6247693>
- [15] —, "Intrinsic scene properties from a single RGB-D image," in *2013 IEEE Conference on Computer Vision and Pattern Recognition, Portland, OR, USA, June 23-28, 2013*. IEEE, 2013, pp. 17–24. [Online]. Available: <http://dx.doi.org/10.1109/CVPR.2013.10>
- [16] —, "Shape, illumination, and reflectance from shading," EECS, UC Berkeley, Tech. Rep. UCB/EECS-2013-117, May 2013.
- [17] P. V. Gehler, C. Rother, M. Kiefel, L. Zhang, and B. Schölkopf, "Recovering intrinsic images with a global sparsity prior on reflectance," in *NIPS*, 2011.
- [18] M. Isard and A. Blake, "CONDENSATION - conditional density propagation for visual tracking," *International Journal of Computer Vision*, vol. 29, no. 1, pp. 5–28, 1998. [Online]. Available: <http://dx.doi.org/10.1023/A:1008078328650>
- [19] S. Thrun, W. Burgard, and D. Fox, *Probabilistic robotics*, 2005.
- [20] G. D. Finlayson, S. D. Hordley, and M. S. Drew, "Removing shadows from images," in *ECCV*, 2002.
- [21] Y. Xiao, E. Tsougenis, and C.-K. Tang, "Shadow removal from single RGB-D images," in *CVPR*. IEEE, 2014.
- [22] S. Fuchs, "Multipath interference compensation in time-of-flight camera images," in *ICPR*, 2010.
- [23] S. Fuchs, M. Suppa, and O. Hellwich, "Compensation for multipath in ToF camera measurements supported by photometric calibration and environment integration," in *Computer Vision Systems*, ser. Lecture Notes in Computer Science, M. Chen, B. Leibe, and B. Neumann, Eds. Springer, 2013, vol. 7963, pp. 31–41.
- [24] D. Jiménez, D. Pizarro, M. Mazo, and S. Palazuelos, "Modeling and correction of multipath interference in time of flight cameras," *Image and Vision Computing*, vol. 32, no. 1, 2014.
- [25] A. Dorrington, J. Godbaz, M. Cree, A. Payne, and L. Streeter, "Separating true range measurements from multi-path and scattering interference in commercial range cameras," vol. 7864, 2011.
- [26] J. P. Godbaz, M. J. Cree, and A. A. Dorrington, "Closed-form inverses for the mixed pixel/multipath interference problem in AMCW lidar," vol. 8296, 2012.
- [27] A. Kirmani, A. Benedetti, and P. A. Chou, "SPUMIC: simultaneous phase unwrapping and multipath interference cancellation in time-of-flight cameras using spectral methods," in *Proceedings of the 2013 IEEE International Conference on Multimedia and Expo, ICME 2013, San Jose, CA, USA, July 15-19, 2013*. IEEE, 2013, pp. 1–6. [Online]. Available: <http://dx.doi.org/10.1109/ICME.2013.6607553>
- [28] D. Freedman, Y. Smolin, E. Krupka, I. Leichter, and M. Schmidt, "SRA: fast removal of general multipath for ToF sensors," in *Computer Vision - ECCV 2014 - 13th European Conference, Zurich, Switzerland, September 6-12, 2014, Proceedings, Part I*, D. J. Fleet, T. Pajdla, B. Schiele, and T. Tuytelaars, Eds. Springer, 2014, pp. 234–249. [Online]. Available: http://dx.doi.org/10.1007/978-3-319-10590-1_16
- [29] D. Wu, M. O'Toole, A. Velten, A. Agrawal, and R. Raskar, "Decomposing global light transport using time of flight imaging," in *CVPR*, 2012.
- [30] A. Bhandari, A. Kadambi, R. Whyte, C. Barsi, M. Feigin, A. Dorrington, and R. Raskar, "Resolving multipath interference in time-of-flight imaging via modulation frequency diversity and sparse regularization," *Optics Letters*, vol. 39, no. 6, pp. 1705–1708, 2014.
- [31] J. Lin, Y. Liu, M. B. Hullin, and Q. Dai, "Fourier analysis on transient imaging with a multifrequency time-of-flight camera," in *CVPR*, 2014.
- [32] M. J. Bayarri and J. O. Berger, "P values for composite null models," *Journal of the American Statistical Association*, vol. 95, no. 452, pp. 1127–1142, 2000.
- [33] E. Tadmor, I. Bakish, S. Felzenshtein, E. Larry, G. Yahav, and D. Cohen, "A fast global shutter image sensor based on the VOD mechanism," in *2014 IEEE Sensors*. IEEE, 2014.

- [34] S. Felzenshtein, G. Yahav, and E. Larry, "Fast gating photosurface," US Patent 8717469, 2014.
- [35] G. Yahav, S. Felzenshtein, and E. Larry, "Capturing gated and ungated light in the same frame on the same photosurface," US Patent Application 20120154535, 2010.
- [36] G. E. Healey and R. Kondepudy, "Radiometric CCD camera calibration and noise estimation," *Pattern Analysis and Machine Intelligence, IEEE Transactions on*, vol. 16, no. 3, pp. 267–276, 1994.
- [37] A. Foi, M. Trimeche, V. Katkovnik, and K. Egiazarian, "Practical Poissonian-Gaussian noise modeling and fitting for single-image raw-data," *IEEE Transactions on Image Processing*, vol. 17, no. 10, pp. 1737–1754, 2008. [Online]. Available: <http://dx.doi.org/10.1109/TIP.2008.2001399>
- [38] D. Scharstein, H. Hirschmüller, Y. Kitajima, G. Krathwohl, N. Nešić, X. Wang, and P. Westling, "High-resolution stereo datasets with subpixel-accurate ground truth," in *Pattern Recognition*. Springer, 2014, pp. 31–42.
- [39] A. Criminisi, J. Shotton, and E. Konukoglu, "Decision forests: A unified framework for classification, regression, density estimation, manifold learning and semi-supervised learning," *Foundations and Trends in Computer Graphics and Vision*, vol. 7, no. 2-3, pp. 81–227, 2012. [Online]. Available: <http://dx.doi.org/10.1561/06000000035>
- [40] R. M. Haralick, "Propagating covariance in computer vision," *IJPRAI*, vol. 10, no. 5, pp. 561–572, 1996. [Online]. Available: <http://dx.doi.org/10.1142/S0218001496000347>
- [41] M. Reynolds, J. Dobos, L. Peel, T. Weyrich, and G. J. Brostow, "Capturing time-of-flight data with confidence," in *CVPR*, 2011.
- [42] A. Gelman and C. R. Shalizi, "Philosophy and the practice of Bayesian statistics," *British Journal of Mathematical and Statistical Psychology*, vol. 66, no. 1, pp. 8–38, 2013.
- [43] D. Lunn, C. Jackson, N. Best, A. Thomas, and D. Spiegelhalter, *The BUGS book: A practical introduction to Bayesian analysis*. CRC Press, 2012.
- [44] X.-L. Meng, "Posterior predictive p-values," *The Annals of Statistics*, pp. 1142–1160, 1994.
- [45] J. M. Robins, A. van der Vaart, and V. Ventura, "Asymptotic distribution of p values in composite null models," *Journal of the American Statistical Association*, vol. 95, no. 452, pp. 1143–1156, 2000.
- [46] J. O. Berger, *Statistical Decision Theory and Bayesian Analysis*. Springer, 1985.
- [47] S. Kirkpatrick, C. D. Gelatt, and M. P. Vecchi, "Optimization by simulated annealing," *Science*, vol. 220, pp. 671–680, 1983.
- [48] W. Jakob, "Mitsuba renderer," 2010, <http://www.mitsuba-renderer.org>.
- [49] E. Veach and L. Guibas, "Bidirectional estimators for light transport," in *Fifth Eurographics Workshop on Rendering*, 1994, pp. 147–162.
- [50] E. Veach and L. J. Guibas, "Metropolis light transport," in *Proceedings of the ACM SIGGRAPH Conference*. ACM Press, 1997, pp. 65–76.
- [51] M. Pharr and G. Humphreys, *Physically based rendering: From theory to implementation*. Morgan Kaufmann, 2010.
- [52] P. Pitts, A. Benedetti, M. Slaney, and P. Chou, "Time of flight tracer," Microsoft Research, Tech. Rep. MSR-TR-2014-142, November 2014.
- [53] A. Jarabo, J. Marco, A. Muñoz, R. Buisan, W. Jarosz, and D. Gutierrez, "A framework for transient rendering," *ACM Transactions on Graphics (SIGGRAPH Asia 2014)*, vol. 33, no. 6, 2014.
- [54] P. A. Dawid, "The well-calibrated Bayesian," *Journal of the American Statistical Association*, vol. 77, no. 379, pp. 605–610, 1982.
- [55] L. N. Trefethen, *Approximation Theory and Approximation Practice*. SIAM, 2012.
- [56] D. C. Liu and J. Nocedal, "On the limited memory BFGS method for large scale optimization," *Mathematical programming*, vol. 45, no. 1-3, pp. 503–528, 1989.
- [57] C. P. Robert, *The Bayesian Choice: From Decision-Theoretic Foundations to Computational Implementation*. Springer, 2001.
- [58] A. C. Genz and A. Malik, "An adaptive algorithm for numerical integration over an n-dimensional rectangular region," *Journal of Computational and Applied Mathematics*, vol. 6, no. 4, pp. 295–302, 1980.
- [59] R. Y. Rubinstein and D. P. Kroese, *Simulation and the Monte Carlo method*. John Wiley & Sons, 2011.
- [60] J. S. Liu, "Metropolized independent sampling with comparisons to rejection sampling and importance sampling," *Statistics and Computing*, vol. 6, no. 2, pp. 113–119, 1996.
- [61] A. Kong, "A note on importance sampling using renormalized weights," Department of Statistics, University of Chicago, Tech. Rep., 1992.
- [62] J. O. Berger *et al.*, "Could fisher, jeffreys and neyman have agreed on testing?" *Statistical Science*, vol. 18, no. 1, pp. 1–32, 2003.
- [63] J. S. Liu, *Monte Carlo Strategies in Scientific Computing*. Springer, 2001.
- [64] P. J. Green, "Reversible jump Markov chain Monte Carlo computation and Bayesian model determination," *Biometrika*, vol. 82, no. 4, pp. 711–732, 1995.
- [65] N. Duffield, C. Lund, and M. Thorup, "Priority sampling for estimation of arbitrary subset sums," *Journal of the ACM (JACM)*, vol. 54, no. 6, p. 32, 2007.



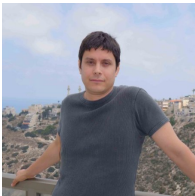
Amit Adam Amit Adam received the PhD degree from the Technion-Israel Institute of Technology in 2001 for a thesis on vision-based navigation. Since his graduation, he has been working as an applied computer vision researcher in various application areas such as medical navigation, video surveillance, and recognition. Joining Microsoft's Advanced Imaging Technologies Group (AIT) in 2012, he has since worked on computational problems related to time-of-flight depth cameras.



Christoph Dann Christoph Dann obtained his B.Sc. and M.Sc. degree in Computer Science from the Technical University of Darmstadt, Germany, in 2011 and 2014, respectively. He is currently working toward a PhD degree in the Machine Learning Department at Carnegie Mellon University, USA. In the past, Christoph worked as an undergraduate researcher at the Max-Planck Institute for Informatics, the Intelligent Autonomous Systems group at the Technical University of Darmstadt, the Aerospace Controls Laboratory at MIT and as a research intern at Microsoft Research, Cambridge, UK. His research primarily focuses on sequential decision making under uncertainty including reinforcement learning as well as applications in computer vision.



Omer Yair received the BSc degree in Electrical Engineering (summa cum laude) and a BSc in Physics (summa cum laude) from the Technion-Israel Institute of Technology in 2011. He is currently with the Advance Imaging Technology Group at Microsoft and pursuing a MSc degree in Physics at the Technion.



Shai Mazor Shai received the B.Sc. and M.Sc. degrees in Electrical Engineering from the Technion-Israel Institute of Technology. After graduating he worked as a developer and later program manager, gaining experience both in startup companies and large corporations. He joined Microsoft's Advanced Imaging Technologies Group (AIT) in 2013, where he is now a senior program manager responsible for incubation of new applications for AIT technology. In addition to his engineering education, Shai holds

an MBA from the IDC, where he was also an exchange student at the Wharton Business School.



Sebastian Nowozin is a researcher in the Machine Learning and Perception group at Microsoft Research Cambridge. He received his Master of Engineering degree from the Shanghai Jiaotong University (SJTU) and his diploma degree in computer science with distinction from the Technical University of Berlin in 2006. He received his PhD degree summa cum laude in 2009 for his thesis on learning with structured data in computer vision, completed at the Max Planck Institute for Biological Cybernetics,

Tübingen and the Technical University of Berlin. His research interest is at the intersection of computer vision and machine learning. He is associate editor for TPAMI, IJCV, and JMLR and regularly serves as PC-member and reviewer for machine learning (NIPS, ICML, AISTATS, UAI, ECML, JMLR) and computer vision (CVPR, ICCV, ECCV, PAMI, IJCV) conferences and journals.

APPENDIX A VIDEO DEMONSTRATION

We submit a short video showing the robustness of our approach. In the video we show robust live (real-time) inference of depth, reflectance/albedo and illumination. We demonstrate the effective separation between illumination and reflectance by waving a powerful light projector and noting that the albedo and depth map stay invariant to the changing illumination conditions.

Please note that the RGB stream was shot by the person holding the light projector - and is unrelated to the depth camera stream (we added it for general impression of the scene - it is slightly confusing).

APPENDIX B INFERENCE DETAILS

For this section we will use the compound parameter vector $\vec{\theta} = [t, \rho, \lambda]^T$, or $\vec{\theta} = [t, \rho, \lambda, t_2, \rho_2]^T$ for the single- and two-paths model. This unifies the notation for all unknown imaging conditions we would like to infer.

The response curve function $\vec{C}(t)$ appearing in the expression for the mean photon response $\vec{\mu}$ (see equation (7) in the main paper), is obtained from calibrated measurements of the actual camera, and then approximated by Chebyshev polynomials of degree sixteen [55]. Because the curves are smooth the Chebyshev approximation is compact yet very accurate and evaluation of $\vec{C}(t)$ also provides the derivatives $\frac{\partial}{\partial t} \vec{C}(t)$ and $\frac{\partial}{\partial z_i} \vec{C}(t)$ for no additional computational cost.

B.1 Maximum Likelihood Estimation (MLE)

The standard maximum likelihood estimate are the imaging conditions t, ρ, λ which maximize the likelihood or equivalently minimize the negative log-likelihood

$$\begin{aligned} \arg\min_{\vec{\theta}} -\log P(\vec{R}|\vec{\theta}) & \quad (24) \\ = \arg\min_{\vec{\theta}} \sum_{i=1}^n \left[\frac{(R_i - \mu_i(\vec{\theta}))^2}{2(\alpha\mu_i(\vec{\theta}) + K)} + \frac{1}{2} \log(\alpha\mu_i(\vec{\theta}) + K) \right]. \end{aligned}$$

With this Chebyshev polynomial approximation we can also compute derivatives with respect to $\vec{\theta}$ of the log-likelihood function, and the entire log-likelihood function becomes smooth and twice differentiable.

Solving the three-dimensional minimization problem in Equation (24) with standard Quasi-Newton methods such as L-BFGS [56] is possible but often yields unreasonable result if we do not constrain the parameters. For example, negative values of ρ might have the lowest function value but are physically impossible. Another issue is that the response curves \vec{C} are measured only within a reasonable range. Outside of this range, the Chebyshev approximations have arbitrary behavior which leads to implausible solutions.

We therefore constrain the range of parameters using log-barrier terms

$$\begin{aligned} \arg\min_{\vec{\theta}} \sum_{i=1}^n \left[\frac{(R_i - \mu_i(\vec{\theta}))^2}{2(\alpha\mu_i(\vec{\theta}) + K)} + \frac{1}{2} \log(\alpha\mu_i(\vec{\theta}) + K) \right] & \quad (25) \\ + \sum_j b (\log(\theta_j - \theta_{j,\min}) + \log(\theta_{j,\max} - \theta_j)). & \quad (26) \end{aligned}$$

The scalar $b = 10^{-2}$ is a *barrier* coefficient and $\vec{\theta}_{\min}, \vec{\theta}_{\max}$ are the smallest and largest values of each parameter we want to consider. The problem remains twice differentiable and quasi-Newton methods can be applied for finding local minima reliably because any local optima has to occur within

the relative interior of the rectangle described by $\theta_{j,\min}$ and $\theta_{j,\max}$.

To find the global optimum, we restart the quasi-Newton method ten times with initialization sampled uniformly in the parameter ranges. For producing labeled training data this is more than sufficient. Even during exposure profile optimization, experiments on good and mediocre shutter designs have shown that after 10 restarts in 97% of the cases the same global solution was found as with 100 restarts.

B.2 Maximum A-Posteriori Estimation (MAP)

The maximum a-posteriori (MAP) estimate is similar to the maximum likelihood estimate but also considers the prior instead of only the likelihood distribution. We determine the estimate by minimizing the negative log posterior

$$\begin{aligned} \arg\min_{\vec{\theta}} -\log P(\vec{\theta}|\vec{R}) & \quad (27) \\ = \arg\min_{\vec{\theta}} \sum_{i=1}^n \left[\frac{(R_i - \mu_i(\vec{\theta}))^2}{2(\alpha\mu_i(\vec{\theta}) + K)} + \frac{1}{2} \log(\alpha\mu_i(\vec{\theta}) + K) \right] \\ - \log p(\vec{\theta}). \end{aligned}$$

Due to the particular choices of twice differentiable prior distributions, we can solve this problem right away with quasi-Newton methods. The log-barrier terms used for the maximum likelihood estimate are now implicitly defined in the prior. In fact, the constrained maximum likelihood estimate in the previous subsection can be understood as MAP estimate with an approximately uniform prior on the ranges $\vec{\theta}_{\min}$ to $\vec{\theta}_{\max}$.

The advantage of the MAP estimate is that when prior knowledge exists - for example a strong belief on the ambient light intensity - then we may incorporate it. In contrast, the MLE does not encode any preference for certain parameter values.

B.3 Bayesian Posterior Inference

The Bayesian point estimate is motivated by statistical decision theory [46, 57]. The Bayes estimator yields the lowest expected error. Assuming the squared loss function, the estimator is characterized as

$$\hat{\theta}_{\text{Bayes}}(\vec{R}) := \arg\min_{\vec{\theta}} \mathbb{E}_{\vec{\theta} \sim P(\vec{\theta}|\vec{R})} [\|\vec{\theta} - \vec{\theta}\|_2^2], \quad (28)$$

where $\vec{\theta}$ are the true but uncertain parameters.

This decision problem has a closed form solution: namely the mean parameters under the marginal posterior distributions. Because the squared loss decomposes over parameters, so does the decision problem.

For example, the Bayes estimator \hat{t}_{Bayes} for depth is given by

$$\hat{t}_{\text{Bayes}}(\vec{R}) = \mathbb{E}[t|\vec{R}] = \int t p(t|\vec{R}) dt. \quad (29)$$

The marginal posterior distribution $p(t|\vec{R})$ can be written in terms of the joint distribution as

$$\begin{aligned} p(t|\vec{R}) &= \int p(\vec{\theta}|\vec{R}) d\vec{\theta} d\lambda \\ &= \int \frac{p(\vec{R}|\vec{\theta})p(\vec{\theta})}{p(\vec{R})} d\rho d\lambda. \end{aligned}$$

The Bayes estimator \hat{t}_{Bayes} is therefore equal to

$$\mathbb{E}[t|\vec{R}] = \frac{\int t p(\vec{\theta})p(\vec{R}|\vec{\theta}) d\vec{\theta}}{\int p(\vec{\theta})p(\vec{R}|\vec{\theta}) d\vec{\theta}}. \quad (30)$$

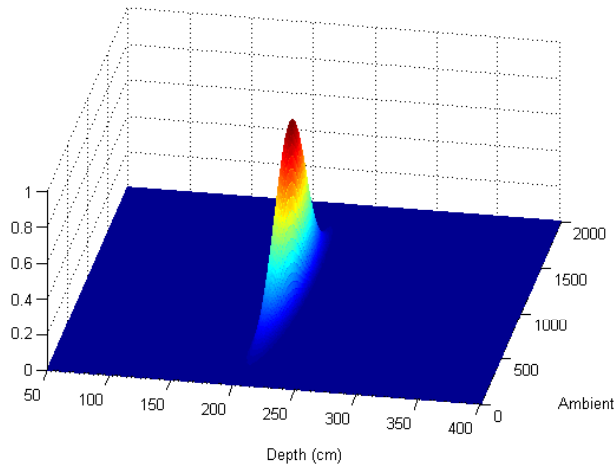


Fig. 17: Slice of the posterior distribution of the single-path model for fixed values of reflectivity ρ . In this case the posterior distribution of the single-path model is dominated by a single Gaussian-like mode.

One way of computing the Bayes estimator is solving the integrals in the numerator and denominator for all parameters that we are interested in. We use a state-of-the-art numerical quadrature method [58] for vector-valued integrals over rectangular regions.

However, the numerical quadrature approach is very slow and has numerical issues that yield sub-optimal solutions. We therefore consider an alternative way to compute the Bayes estimators: Monte Carlo using importance sampling [59].

We observed that the posterior distributions of the single-path model are mostly dominated by a few important modes that often have symmetric shape, see Figure 17. The posterior can therefore be approximated well by a mixture of Gaussians. Using importance sampling with a mixture of Gaussians proposal distribution should therefore yield fast convergence to the true Bayes estimator.

The proposal distribution is a mixture of k Gaussians placed at the outputs of k local optima of the MAP problem obtained as described in Section (B.2). The proposal distribution is

$$q(\vec{\theta}) \propto \sum_{i=1}^k p(\vec{\theta}^{(i)}) p(\vec{R}|\vec{\theta}^{(i)}) \mathcal{N}(\vec{\theta}|\vec{\theta}^{(i)}, H^{(i)}), \quad (31)$$

where k is the number of mixture components used and $\vec{\theta}^{(k)}$ are the locations of these mixtures. For the covariance matrices $H^{(k)}$ we use the inverse Hessian of the negative log-posterior (as in a Laplace approximation). Due to the particular choice of twice differentiable priors, the Hessian of the log-posterior are always positive definite in local optima.

We generate samples $\vec{\eta}_1 \dots \vec{\eta}_m$ from q and re-weight each sample by $w_i = \frac{p(\vec{\eta}_i)}{q(\vec{\eta}_i)}$ to account for the errors in the approximation of the posterior by q . These samples are then used to obtain Monte-Carlo estimates of the integrals in equation (30).

We determine the number of samples required to approximate the integrals by the *effective sample size* (ESS) [60, 61],

$$\frac{(\sum_{i=1}^m w_i)^2}{\sum_{i=1}^m w_i^2}. \quad (32)$$

We stop sampling as soon as the ESS exceeds a threshold (usually in the order of 50–200). In most cases this threshold is reached with a small number of actual samples. Empirically we observe the importance sampling approach to be much faster and robust in practice than the numerical quadrature approach.

APPENDIX C TEST-TIME REGRESSION TREE INFERENCE DETAILS

The regression trees approach we described in the main paper has an advantage in terms of flexibility. We used this flexibility to solve several issues that we encountered during development of the prototype camera. While a full description of the issues and their seamless solution within this framework is beyond the scope of this paper, we want to provide one important example.

One notes that all inference is based on the response curve $\vec{C}(\cdot)$ which characterizes the pixel’s response to depth. In the physical camera, due to various optical and semiconductor effects, this response curve varies between sensor elements, and this variation is smooth with the position of the pixel on the image sensor. As a result, instead of having a single curve $\vec{C}(\cdot)$ as we described so far, we actually have a set of response curves $\vec{C}_{x,y}(\cdot)$, one for each pixel in the image. Using the regression tree framework, we had a simple seamless solution for this issue as follows:

- During training, instead of sampling responses from a single curve $\vec{C}(\cdot)$, we sample responses from multiple response curves corresponding to different parts of the image. To obtain the label $\hat{t}(\vec{R}_i)$, use slow inference with the actual (position dependent) curve from which \vec{R}_i was sampled.
- We augment the feature vector to include pixel position in addition to the response \vec{R} .
- We extend the leaf model and add linear terms in pixel coordinates x and y .
- Train the regression tree as usual.
- During runtime: just add pixel position to the feature vector used to traverse the tree

This example serves to show the added benefit of a flexible regression mechanism in extending the model to solve new and unexpected problems.

APPENDIX D MODEL CHECKING AND P-VALUES

This discussion provides additional background for our choice of the posterior predictive p-value used in the main paper. P-values are highly controversial in the field of statistics, in particular for formal hypothesis testing. For example, in [44] Xiaoli Meng writes about the p-value,

“There is perhaps no single notion in statistics, other than the p -value, that has been so widely used and yet so seriously criticized for so long.”

Many works have discussed this controversy and Berger [62] provides a nice formal summary of the issues of disagreement.

For models that are fully observed the choice of a test statistic unambiguously defines the p-value. However, our model involves unobserved quantities, the imaging conditions t , ρ , and λ , as well as t_2 and ρ_2 for the two-path model. In this case, there is no single p-value to be used and this case is known as “composite null hypothesis” or models with “nuisance parameters”. Also, in this case the test statistic in the classical p-value generally does not depend on the nuisance parameter, which is a drawback as it limits the choice of useful test statistics.

The posterior predictive p-value [32, 44] addresses both problems by integrating the test statistic over the Bayesian posterior of the unknown variables. As test statistic we choose the likelihood of the observation given the unknown parameters, yielding equation (16) in the main paper.

It is easier to understand the usefulness of the likelihood as a test statistic on a model that is fully observed. We visualize such an example with a simple Gaussian mixture model in Figure 18. For the case with unobserved variables the situation is similar except that the distribution changes as a function of the observation \vec{R} .

The posterior predictive p-value has known drawbacks, analyzed in [32, 45]. In particular it is known that it can be too conservative in rejecting the null hypothesis. In our application this implies that we may not detect all detectable deviation from the assumed model. Intuitively the reason for this lack of power is that the p-value is not Bayesian and actually does use the observation twice, once to define the posterior, and once in the computation that defines the p-value, leading to overly optimistic agreement with the model. The so called *partial* posterior predictive p-value [32] does successfully address this issue but it is much more difficult to compute; in fact, although desirable, we have not found a practical method to compute it in our application.

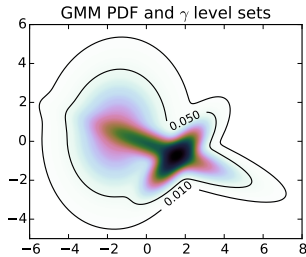


Fig. 18: Invalidation score example. For a Gaussian mixture model level sets at significance levels $\gamma \in \{0.01, 0.05\}$ separate the total probability mass such that outside the level set the integrated probability is γ . Samples outside these sets are rejected.

APPENDIX E EXPOSURE PROFILES DESIGN DETAILS

To optimize the design objective (19) in the main paper, we use a simulated annealing approach as follows. Let us abbreviate the objective function (19) as

$$f(\mathbf{Z}) = \mathbb{E}_{t, \rho, \lambda} \mathbb{E}_{\vec{R} \sim P(\vec{R}|t, \rho, \lambda, \mathbf{Z})} \left[\ell(\hat{t}(\vec{R}), t) \right]. \quad (33)$$

We introduce an auxiliary Gibbs distribution, parametrized by a temperature $T > 0$,

$$r(\mathbf{Z}, T) \propto \exp\left(-\frac{1}{T} f(\mathbf{Z})\right). \quad (34)$$

We use a sequence of temperature parameters that is slowly decreased for a finite number of steps, that is, $T_0 > T_1 > \dots > T_K$, starting from an initial temperature $T_0 = T_{\text{start}}$ down to a final temperature $T_K = T_{\text{final}}$. The smaller T gets, the more peaked the distribution $r(\cdot, T)$ becomes around the minimum of f . Given a Markov chain sampler on r , this approach converges to the global minimum of f .

We first discuss the Markov chain that we use, then give details about the temperature schedule.

E.1 Markov Chain

To account for the sparsity constraints on \mathbf{Z} , our Markov chain uses an augmented state space [63] to avoid measure-theoretic difficulties of asserting reversibility in the context of changing dimensionality [64].

We decompose \mathbf{Z} into a binary matrix $\mathbf{B} \in \{0, 1\}^{m \times n}$ and a value matrix $\mathbf{V} \in \mathbb{R}^{m \times n}$ with $Z_{ji} = B_{ji}V_{ji}$. This allows us to easily set weights to zero by setting $B_{ji} = 0$ and have the reversible proposal readily available by setting $B_{ji} = 1$. Our MCMC sampler is a reversible Metropolis-Hastings sampler and consists of the following transition kernels (moves):

- 1) *Move mass*: Choose two matrix entries V_{ji}, V_{kl} randomly (uniform) and move a uniformly sampled value from one

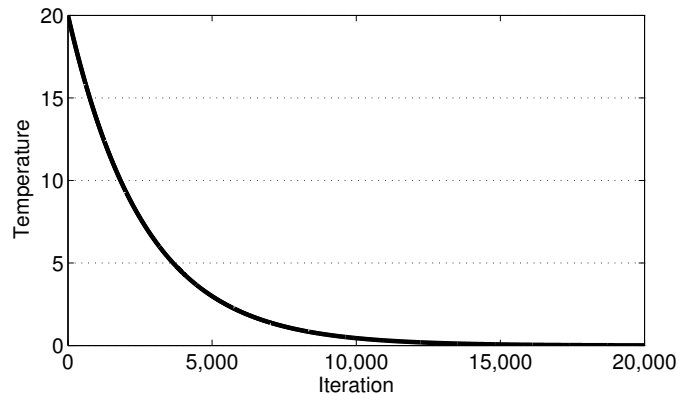


Fig. 19: Simulated annealing schedule used during shutter profile design optimization, here with $K = 20,000$ iterations.

entry to another such that their total value stays the same and both are still positive. This kernel is reversible with itself.

- 2) *Swap values*: Choose two matrix entries W_{ji}, W_{ji} randomly (uniform) and swap their values V and binary indicator value B . This kernel is reversible with itself.
- 3) *Set a weight to zero*: Choose a matrix entry with $B_{ji} = 1$ randomly (uniform) and set it to zero. This kernel is reversible with the following kernel.
- 4) *Set a weight to nonzero*: Choose a matrix entry with $B_{ji} = 0$ randomly (uniform) and set its binary indicator value to one. This kernel is reversible with the previous set-to-zero kernel.
- 5) *Perturb weight value*: Choose a matrix entry $V_{ji} = 0$ randomly (uniform) and rescale its value with a log-normal sampled factor. This kernel is reversible with itself.
- 6) *Scale all weight values*: Rescale all values \mathbf{V} with a log-normal sampled scalar. This kernel is reversible with itself.

The above kernels are combined with the following probabilities: 20% for the *move mass* kernel; 20% for the *swap values* kernel; 10% for the *set-to-zero* and *set-to-nonzero* kernels, each; 30% for the *perturb weight* kernel; 10% for the *global scaling* kernel.

E.2 Temperature Schedule

For simulated annealing we use a geometric temperature schedule [47], with the temperature at iteration k being

$$T_k = T_{\text{start}} \beta^k,$$

where we use the initial temperature $T_{\text{start}} = 20$ and a target temperature of $T_{\text{final}} = 0.01$, so that

$$\beta = \exp\left(\frac{1}{K} [\log T_{\text{final}} - \log T_{\text{start}}]\right).$$

This leads to the schedule as shown in Figure 19. We typically use a $K = 20,000$ or $K = 100,000$ iterations.

APPENDIX F TIME OF FLIGHT SIMULATION DETAILS

We now discuss details of the physically accurate light simulation that we use to simulate multipath phenomena. First we recap the basis of both the bidirectional path tracer (BDPT) and the Metropolis light transport (MLT) algorithms [49, 50] and then provide information about the variance reduction techniques we use.

F.1 Light Transport Formulation

Assuming a geometric light model where light travels in straight lines and only interacts with surfaces, the measured light intensity at a pixel in a static scene without active illumination can be formulated as a path integral. This integral accumulates the intensity from light paths $x_0, x_1 \dots x_{k+1}$ that start in a point x_0 on an emitting surface and end in a point x_{k+1} on the pixel's sensor surface. The intermediate nodes of this path $x_1 \dots x_k$ are surfaces in the scene. The integral can be formulated (see [50] for details) as

$$\sum_{k=0}^{\infty} \int_{\mathcal{M}^{k+1}} L_e(x_0 \rightarrow x_1) G(X_0 \leftrightarrow x_1) \prod_{i=1}^k (f(x_{i-1} \rightarrow x_i \rightarrow x_{i+1}) G(x_i \leftrightarrow x_{i+1})) L_s(x_k \rightarrow x_{k+1}) dA(x_0) \dots dA(x_{k+1}). \quad (35)$$

In this equation,

- \mathcal{M} is the set of all surfaces in the scene including emitters and the camera sensor and A is the area measure on \mathcal{M} ;
- $L_e(x_0 \rightarrow x_1)$ is a function representing emitters. It is proportional to the light that is emitted from point x_0 in the direction of x_1 . It takes only non-zero values if x_0 is on emitter surfaces;
- $L_s(x_k \rightarrow x_{k+1})$ is the equivalent of L_e for the sensor. L_s specifies how sensitive the sensor is for photons arriving at x_{k+1} from the direction of x_k .
- $f(x_{i-1} \rightarrow x_i \rightarrow x_{i+1})$ is the bidirectional scattering distribution function (BSDF) describing how much light is scattered at surface point x_i in direction x_{i+1} of an incoming ray from the direction of x_{i-1} ;
- $G(x_i \leftrightarrow x_{i+1}) = V(x_i \leftrightarrow x_{i+1}) \frac{|\cos \phi_i \cos \phi_{i+1}|}{\|x_{i+1} - x_i\|^2}$ is the throughput of a differential beam between $dA(x_i)$ and $dA(x_{i+1})$. $V(x_i \leftrightarrow x_{i+1})$ is an indicator function for mutual visibility of x_i and x_{i+1} , which means V is zero if the direct path between the two inputs is blocked, otherwise 1; The variables ϕ_i, ϕ_{i+1} denote the angle between the beam and the surface normals at x_i and x_{i+1} .

The observed response in a specific pixel of our time-of-flight camera from the emitted light pulse can be modelled by extending the path integral formulation above to

$$R_{\text{active}} = \int \sum_{k=0}^{\infty} \int_{\mathcal{M}^{k+1}} P(u) L_e(x_0 \rightarrow x_1) G(X_0 \leftrightarrow x_1) \prod_{i=1}^k (f(x_{i-1} \rightarrow x_i \rightarrow x_{i+1}) G(x_i \leftrightarrow x_{i+1})) L_s(x_k \rightarrow x_{k+1}) S_j(u + t_l) dA(x_0) \dots dA(x_{k+1}) du. \quad (36)$$

We additionally integrate over time u and include the intensity of the emitted pulse $P(t)$ as well as the shutter function $S_j(t + t_l)$. The time delay $t_l = cl$ of emitted light arriving at the sensor is the total path length,

$$l = \sum_i \|x_{i+1} - x_i\|,$$

times the speed of light c . All terms involving time can be group together into the expression

$$\int P(u) S_j(u + t_l) du = \frac{C_j(t_l)}{d(t_l)}$$

that only depends on the time delay t_l corresponding to total path length. It corresponds to the curve C_j without the decay of light $d(t_l)$ due to distance l (The decay of light is already

accounted for in the G terms of the integral). The measured response is then

$$R_{\text{active}} = \sum_{k=0}^{\infty} \int_{\mathcal{M}^{k+1}} \frac{C_j(t_l)}{d(t_l)} L_e(x_0 \rightarrow x_1) G(X_0 \leftrightarrow x_1) \prod_{i=1}^k (f(x_{i-1} \rightarrow x_i \rightarrow x_{i+1}) G(x_i \leftrightarrow x_{i+1})) L_s(x_k \rightarrow x_{k+1}) dA(x_0) \dots dA(x_{k+1}). \quad (37)$$

This formulation is identical to the path integral Equation (35) but with the additional $C_j(t_l)/d(t_l)$ term.

We modified the bidirectional path tracer (BDPT) algorithm [49] and the Metropolis light transport (MLT) algorithm [50] in the Mitsuba renderer [48] to produce a weighted set of samples $\{(w_i, L_i, t_i)\}_{i=1, \dots, N}$ of the path integral in Equation (35). The weight of the path sample is w_i , L_i is the number of edges and t_i is the time corresponding to the total path distance. We can generate samples of R_{active} by

$$\sum_{i=1}^N \frac{w_i}{d(t_i)} C_j(t_i).$$

Considering all shutters C_1, C_2, \dots and adding constant ambient light τ to account for R_{ambient} , we may obtain realistic estimates of the mean response vector

$$\vec{\mu} = \tau \vec{A} + \sum_{i=1}^N \frac{w_i}{d(t_i)} \vec{C}(t_i). \quad (38)$$

F.2 Variance Reduction

The BDPT and MLT rendering techniques are Monte Carlo methods and therefore estimates obtained from them will have a Monte Carlo variance. This variance does not originate with the underlying mechanism that is being simulated, but is due to the finite number of samples that are used for estimation. Whereas normal light transport rendering in computer graphics applications is targeted at estimating mean intensities in three spectral bands (RGB), we are instead interested in the time-of-flight density. Because it is a function instead of a small number of values, it is more difficult to obtain reliable estimates of this function.

To improve the accuracy of our estimate with the given time and memory constraints, we use two variance reduction techniques: *stratification* and *priority sampling*.

The starting point for both methods is a stream of weighted samples (w_i, L_i, t_i) being generated for each pixel.

F.2.1 Stratification

Stratification is a classic variance reduction technique based on prior knowledge of subpopulations which have lower within-population variation. It works by breaking up the estimation problem into one estimation problem per subpopulation and combining the individual estimates into one joint estimate. This reduces the variance of the joint estimate compared to lumping all subpopulations together in only one population and sampling and estimating from only this one population [59, Section 5.5].

We *stratify* the incoming stream of samples into two sets. The first stratum is the set of samples $L_i = 2$ and the second stratum is the set of samples for which $L_i > 2$. For both sets we keep an equal number of samples, typically a few thousand. The following priority sampling is then performed on each of these two sets separately.

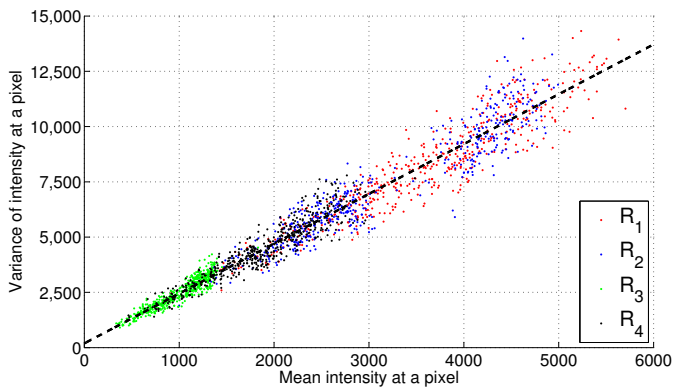


Fig. 20: Validation of the noise model (8). The variance of the response is approximately a linear function of the mean response [37]. We show samples from four responses in different colors and superimpose the least squares fit.

F.2.2 Priority Sampling

The output of the simulation is a set of path samples (w_i, L_i, t_i) for each pixel. For large image sizes this can require tens of gigabytes of storage. In particular for the MLT sampler many of these samples contain partially redundant information due to correlated sampling via running a Markov chain, and storing all of them is wasteful in terms of storage. Because for MLT the samples are correlated in time, one really does need to generate a large number of samples to get good estimates; it is only the storage that is wasteful. For BDPT the samples are uncorrelated but we can still improve estimates by replacing low-weight samples with more important ones due to the inefficiencies of importance sampling.

Typically, in general Markov chain Monte Carlo simulations the samples are unweighted and one can simply *thin* the samples by taking, for example, every 10th sample only, or by using reservoir sampling to keep a random subset. Here, however, the samples from both BDPT (importance sampling) and MLT (Markov chain simulations) are weighted, and this naive strategy—while still valid in terms of providing an unbiased estimate—yields a high variance estimate because it discards important samples with high weights.

To obtain low-variance estimates from few samples we use *priority sampling* [65], a close to optimal method addressing the above subsampling problem. Intuitively, priority sampling generalizes reservoir sampling to the case of weighted samples. It processes the input sample stream one sample at a time and keeps a fixed number of samples with adjusted weights. The weights are adjusted such that the estimate of any subset sum is unbiased, and the variance of weight subset sums is almost optimal uniformly over all possible subsets.

We use priority sampling to thin the two sample streams for each stratum and after rendering is finished we simply output the kept samples and adjusted weights.

Overall we found that the bidirectional path tracer (BDPT) often produces better results with lower variance and all simulation results in the main paper are obtained by running BDPT with 8192 samples per pixel.

APPENDIX G NOISE MODEL VALIDATION

To verify the noise model we assumed in Section 3 (equation 8) of the main paper, we used the experimental setup as described in Section 9.2 of the main paper: we sample 500 random pixels and capture 200 frames from a static scene. We then measure the variance of each pixel’s response, as well as estimate the mean response; this provides empirical data about the actual noise present in the input signal.

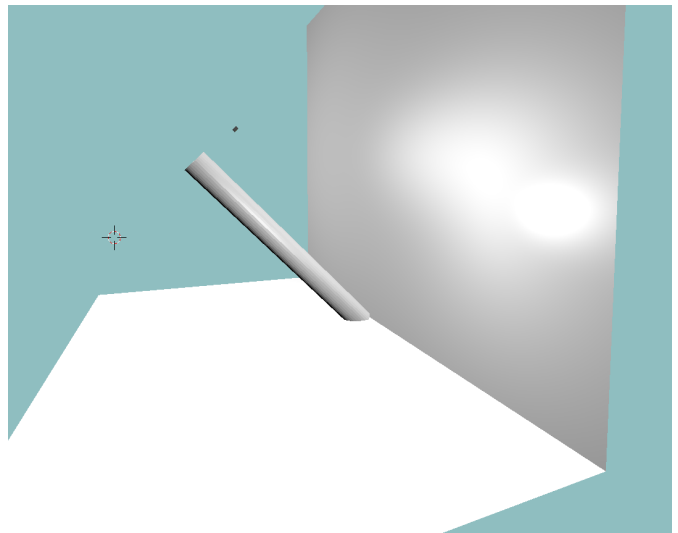


Fig. 21: The scene used for designing a multipath-resistant exposure profile.

Figure 20 shows the noise model results in the form of a scatter plot of the variance of responses versus their mean. The data clearly validates the assumed noise model (8) from the main paper, and shows that the signal-dependent Poissonian shot noise component dominates except for very small intensities.

APPENDIX H THE SCENE USED AS AN EXTENDED GENERATIVE MODEL

As described in Section 8.3 in the main paper, we may use a realistic light transport simulation as a more complex generative model Q in order to generate responses containing also multipath components. We used this method to design a multipath-resistant exposure profile. The scene we used is depicted in Figure 21. The camera is pointed towards a reflective wall, and the responses sampled from the cylinder and the floor contain both a direct component and multipath components. We used two copies of this scene at two different scales. The exposure profile designed using this scene was tested on a very different test scene as described in Section 9.5.

APPENDIX I ADDITIONAL RENDERED RESULTS

In Section 9.8 of the main paper we omitted three scenes for space reasons; the results are provided here in Figure 22, Figure 23, and Figure 24 and qualitatively agree with the results shown in the main paper.

I.1 Example Problem with γ

We now give an example where we suffer high depth errors but have no operational method to recognize this: the estimated uncertainty $\hat{\sigma}$ is not overly large, and the invalidation score γ does not indicate deviation from the model.

The situation occurs in the scene shown in Figure 23, and we highlight the area in Figure 25. In essence the problem is due to complex multipath phenomena involving diffuse multipath and multiple bounces as can be seen from Figure 25(b), which leads to an observed response that is well within a high-probability region of the assumed two-path model (no invalidation) and has a strong direct response component (leading to low $\hat{\sigma}$).

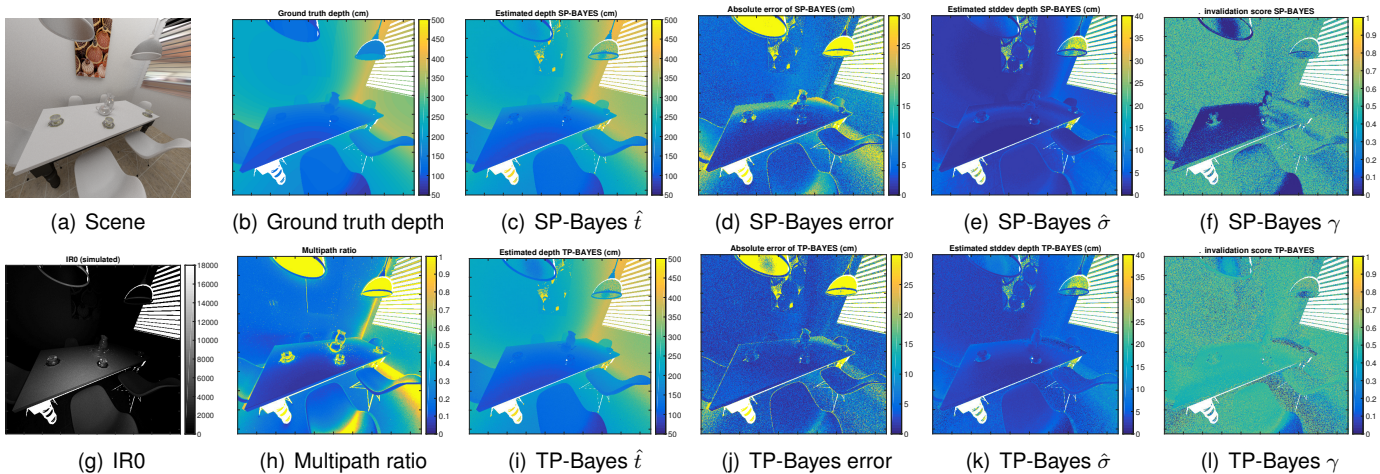


Fig. 22: Rendered simulation (scene adapted from “The Breakfast Room” by Wig42, licensed CC-BY from blendswap.com). Significant multipath error reductions due to the two-path model are visible (wall, table, floor, chairs). Specular surfaces (lamp shade) remain problematic.

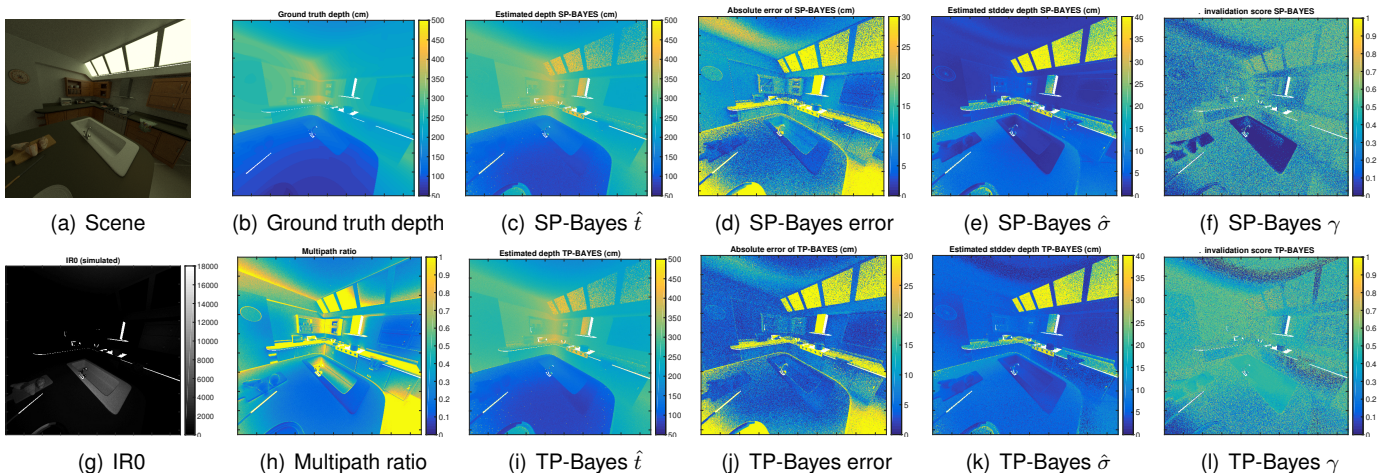


Fig. 23: Rendered simulation (scene adapted from “Kitchen Nr 2” by oldtime, licensed CC-BY from blendswap.com).

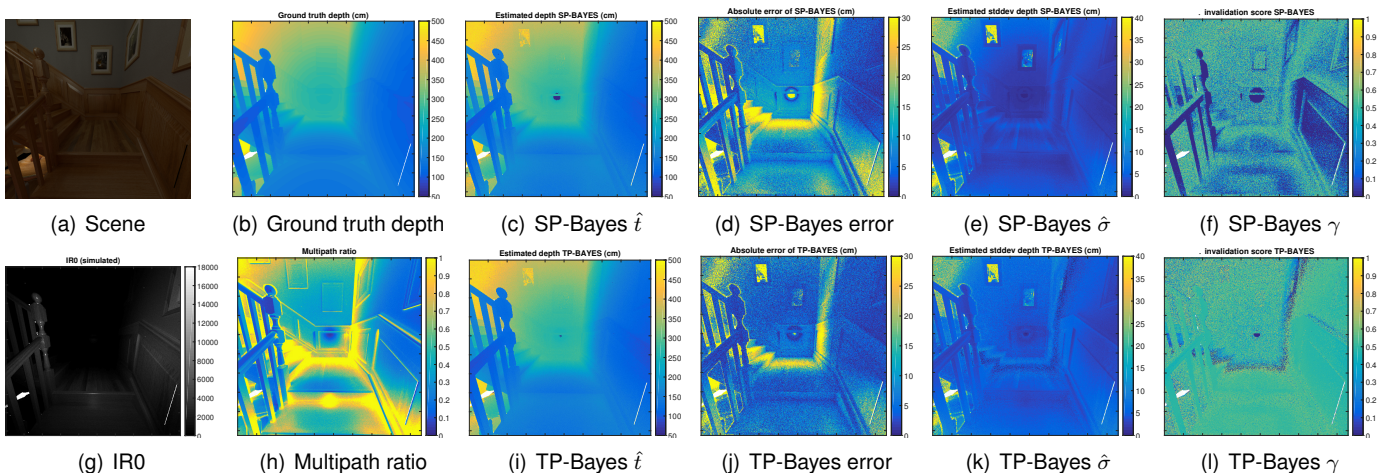
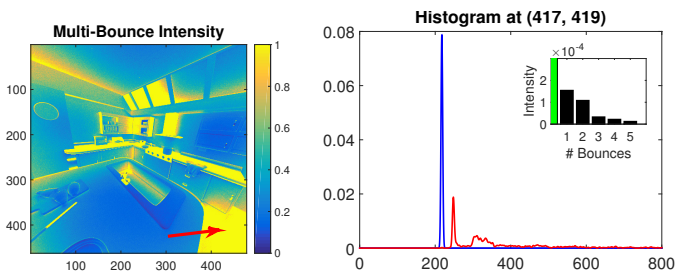


Fig. 24: Rendered simulation (scene adapted from “The Wooden Staircase” by Wig42, licensed CC-BY from blendswap.com).

In order to improve depth accuracy in regions such as the highlighted one, several approaches are relevant. We are currently considering temporal integration of the observed response and an imaging model that does not assume conditional independence among different sensor elements. For

example, many surfaces are planar and recognizing deviations from planarity over multiple pixels could potentially provide a strong cue to recognize and correct for multipath interference.



(a) Problematic area with high depth error (see Fig. 23(j)) that is not recognized by $\hat{\sigma}$ (see Fig. 23(k)), nor by γ (see Fig. 23(l)).

(b) Intensity measure at the highlighted pixel showing complex multipath phenomena with more than two-path responses and large diffuse multipath.

Fig. 25: Explaining a failure of $\hat{\sigma}$ and γ to recognize areas of large depth errors.